



# 1 **Transport-driven aerosol differences above and below the canopy of** 2 **a mixed deciduous forest**

3 Alexander A.T. Bui<sup>1</sup>, Henry W. Wallace<sup>1, a</sup>, Sarah Kavassalis<sup>2</sup>, Hariprasad D. Alwe<sup>3</sup>, James H. Flynn<sup>4</sup>,  
4 Matt H. Erickson<sup>4, b</sup>, Sergio Alvarez<sup>4</sup>, Dylan B. Millet<sup>3</sup>, Allison L. Steiner<sup>5</sup>, Robert J. Griffin<sup>1, 6</sup>

5 <sup>1</sup> Department of Civil and Environmental Engineering, Rice University, Houston, TX, 77005, USA

6 <sup>2</sup> Department of Chemistry, University of Toronto, Toronto, ON, M5S 3H6, Canada

7 <sup>3</sup> Department of Soil, Water, and Climate, University of Minnesota, St. Paul, MN 55108, USA

8 <sup>4</sup> Department of Earth and Atmospheric Sciences, University of Houston, Houston, TX, 77204, USA

9 <sup>5</sup> Department of Climate and Space Sciences and Engineering, University of Michigan, Ann Arbor, MI, 48109, USA

10 <sup>6</sup> Department of Chemical and Biomolecular Engineering, Rice University, Houston, TX, 77005, USA

11 <sup>a</sup> now at: Washington State Department of Ecology, Lacey, WA, 98503, USA

12 <sup>b</sup> now at: TerraGraphics Environmental Engineering, Pasco, WA, 99301, USA

13 *Correspondence to:* Robert J. Griffin (rob.griffin@rice.edu)

14 **Abstract.** Exchanges of energy and mass between the surrounding air and plant surfaces occur below, within, and above a  
15 forest's vegetative canopy. The canopy also can lead to vertical gradients in light, trace gases, oxidant availability, turbulent  
16 mixing, and properties and concentrations of organic aerosols (OA). In this study, a high-resolution time-of-flight aerosol  
17 mass spectrometer is used to measure non-refractory submicron aerosol composition and concentration above (30m) and  
18 below (6m) a forest canopy in a mixed deciduous forest at the Program for Research on Oxidants: Photochemistry,  
19 Emissions, and Transport tower in northern Michigan during the summer of 2016. Three OA factors are resolved using  
20 positive matrix factorization: more-oxidized oxygenated organic aerosol (MO-OOA), isoprene-epoxydiol-derived organic  
21 aerosol (IEPOX-OA), and 91Fac (a factor characterized with a distinct fragment ion at  $m/z$  91) from both the above- and  
22 below-canopy inlets. MO-OOA was most strongly associated with long-range transport from more polluted regions to the  
23 south, while IEPOX-OA and 91Fac were associated with shorter-range transport and local oxidation chemistry. Overall  
24 vertical similarity in aerosol composition, degrees of oxidation, and diurnal profiles between the two inlets was observed  
25 throughout the campaign, which implies that rapid in-canopy transport of aerosols is efficient enough to cause relatively  
26 consistent vertical distributions of aerosols at this scale. However, four distinct vertical gradient episodes are identified for  
27 OA, with vertical concentration differences (above-canopy minus below-canopy concentrations) in total OA of up to 0.8  
28  $\mu\text{g}/\text{m}^3$ . The magnitude of these differences correlated with concurrent vertical differences in either sulfate aerosol or ozone.  
29 These differences are likely driven by a combination of long-range transport mechanisms, canopy-scale mixing and local  
30 chemistry. These results emphasize the importance of including vertical and horizontal transport mechanisms when  
31 interpreting trace gas and aerosol data in forested environments.

32



### 33 1 Introduction

34 Aerosols play a key role in the energy balance of the Earth's climate system by scattering and absorbing incoming solar  
35 radiation and by impacting cloud lifetime and reflectivity (IPCC, 2007). These climatic effects depend strongly on the  
36 chemical speciation of the aerosol particles. Approximately 20-90% of submicron aerosol mass worldwide on average has  
37 been predicted to be organic material (Kanakidou et al., 2005), and this is supported by field studies in a variety of urban,  
38 urban downwind, and rural locations across the Northern Hemisphere (Jimenez et al., 2009; Zhang et al., 2007). The bulk of  
39 this organic material is thought to be secondary organic aerosol (SOA), which is formed in the atmosphere by the reaction of  
40 volatile organic compounds (VOCs) with oxidants such as hydroxyl radical (OH), ozone (O<sub>3</sub>), nitrate radical, and chlorine  
41 atom, with the resulting products then partitioning to the particle phase.

42 Precursor VOCs that contribute to SOA formation are emitted from both anthropogenic and biogenic sources. Biogenic  
43 VOCs (BVOCs) primarily are emitted into the atmosphere from terrestrial vegetation, and on a global scale, emissions of  
44 BVOCs exceed those of anthropogenic VOCs (Fehsenfeld et al., 1992; Guenther et al., 2000, 1995). Major SOA precursor  
45 BVOCs include isoprene (C<sub>5</sub>H<sub>8</sub>) and terpenes. To date, more than 5000 terpene compounds have been identified, including  
46 monoterpenes (C<sub>10</sub>), sesquiterpenes (C<sub>15</sub>), and diterpenes (C<sub>20</sub>) (Geron et al., 2000). However, factors such as the addition  
47 of functional groups (aldehydes, alcohols, carboxylic acids, alkyl nitrate, etc.) and the wide variety of possible reaction  
48 pathways rapidly increase the number of relevant atmospheric VOCs beyond what is initially emitted (Goldstein and  
49 Galbally, 2007).

50 If other loss processes, including deposition, were not considered, the final atmospheric fate of the carbon associated  
51 with BVOCs would be oxidation to carbon dioxide. However, partitioning of oxidation products to the aerosol phase as  
52 SOA interrupts this oxidation sequence. Partitioning of VOC oxidation products between the gas and aerosol phases  
53 depends on multiple factors such as the phase and concentration of pre-existing primary OA (POA) or SOA, particulate-  
54 phase SOA reactions, and the presence of aerosol liquid water (ALW) (Seinfeld and Pandis, 2006). As a result of the large  
55 number of precursor VOCs, the highly non-linear oxidation chemistry, and the presence of multiple aerosol phases in the  
56 atmosphere, SOA formation is complex and relatively poorly understood (Goldstein and Galbally, 2007).

57 The physical environment strongly impacts these chemical SOA formation processes. For example, in forested areas in  
58 which BVOC emissions are prevalent, the exchanges of energy and mass between the forest and the atmosphere are  
59 influenced by the forest's vegetation canopy. Absorption of light by a canopy can diminish the amount of radiation that is  
60 received below the canopy, influencing photolysis rates of photolabile species (Baldocchi et al., 1995; Brown et al., 2005;  
61 Fuentes et al., 2007; Makar et al., 2017; Schulze et al., 2017) and oxidant availability (Fuentes et al., 2007). Loss of BVOC  
62 oxidation products to deposition within the canopy also has been found to be an important factor in determining the  
63 oxidative capacity of a forested environment (Pugh et al., 2009).

64 Vertical transport, also influenced by the canopy, likewise impacts the concentrations of BVOC and SOA in forested  
65 environments. Roughness elements created by the leaves, branches, and stems in a dense vegetative canopy combined with  
66 above-canopy wind shear leads to coherent structures (Finnigan, 2000). These turbulent flow structures contribute to the  
67 fluxes of heat, energy, and matter in forest canopies (Thomas and Foken, 2007). The physical motion of coherent structures  
68 occurs via two main mechanisms: upward "bursts," in which air is ejected upward from the canopy into the atmosphere, and  
69 downward "sweeps," in which air is directed downward from the atmosphere into the canopy. Vertically resolved sonic  
70 anemometer measurements, which provide temperature and three-dimensional wind velocity components at each vertical  
71 measurement location, can be used to derive in-canopy mixing metrics.

72 The relative magnitudes of timescales for turbulent transport and chemical processing govern how trace compounds are  
73 distributed within the canopy (Baldocchi et al., 1995; Fuentes et al., 2007; Steiner et al., 2011). A modeling study by Gao et  
74 al. (1993) found that in-canopy chemical processing of isoprene occurs on a much longer timescale than turbulent transport,  
75 making in-canopy reactions less important compared to the turbulent transport and emission of isoprene in determining its



76 in-canopy concentrations. On the other hand, for compounds with an estimated chemical loss timescale that is roughly  
77 equivalent to the timescales of turbulent transport (e.g., O<sub>3</sub>-initiated oxidation of the sesquiterpene β-caryophyllene), rapid  
78 in-canopy chemical loss could dominate (Stroud et al., 2005). Furthermore, partitioning to the aerosol-phase was inferred as  
79 a potential reason for observations of decreased mixing ratios of oxidation products of very reactive BVOCs in a ponderosa  
80 pine forest canopy (Holzinger et al., 2005).

81 Several studies have attempted to model vertical profiles of trace gases and aerosols in a forest canopy considering both  
82 chemistry and turbulent transport. Bryan et al. (2012) found that forest canopy-atmosphere interactions were highly  
83 sensitive to turbulent mixing parameterizations during a field campaign in northern Michigan. Differences in highly reactive  
84 BVOCs and BVOC oxidation products have been estimated above and below the canopy in modeling and measurement  
85 efforts (Alwe et al., 2019; Ashworth et al., 2015; Holzinger et al., 2005; Schulze et al., 2017; Stroud et al., 2005; Wolfe and  
86 Thornton, 2011). Schulze et al. (2017) found that rapid through-canopy transport (minimum in-canopy residence time of 10  
87 min) leads to relatively consistent simulated above- and below-canopy SOA composition and concentration.

88 Because in-canopy mixing plays a role in the vertical distribution of trace gases and aerosols in a forest canopy, vertical  
89 differences in OA components and other inorganic aerosol species such as sulfate (SO<sub>4</sub>) could be caused by the degree of  
90 mixing between the above- and below-canopy environments. During the PROPHET-CABINEX 2009 campaign, the degree  
91 of atmosphere-canopy coupling between the above-canopy atmosphere and the forest was analyzed by Steiner et al. (2011).  
92 In this study, the degree of coupling was calculated using the ratio of the kinematic heat flux above the canopy to the  
93 kinematic heat flux in the upper canopy. Opposing kinematic heat flux directions (negative ratios) imply that the below-  
94 canopy environment is uncoupled from the atmosphere. In 2009, coupling conditions ranged between strong coupling, weak  
95 coupling, and uncoupled. Uncoupled conditions occurred most commonly in the early morning hours between 4AM and  
96 8AM local time. This set of hours represents approximately 30% of every day over the whole 2009 study period. This  
97 suggests that early morning hours may contribute to more instances of uncoupled canopy-atmosphere conditions but that  
98 coupling between the forest canopy and the atmosphere occurs a majority of the time (Steiner et al., 2011).

99 Past field studies, such as those above a tropical forest in Brazil and a temperate forest in California, found that in-  
100 canopy SOA formation, deposition, and thermal gradient effects on gas-particle partitioning all influence net OA fluxes  
101 (Farmer et al., 2013). In the same study, the authors found that oxygenated OA tended to deposit in the canopy, whereas the  
102 forest canopy released less oxygenated OA. The source of OA fluxes between forests and the atmosphere has been  
103 associated with vertical turbulent transport between the forest atmosphere and the surface layer directly above the canopy;  
104 however, there have been few studies that have provided high temporal resolution measurements of both OA composition  
105 throughout a forest canopy and canopy mixing strength. In a mixed forest in Ontario, Canada, Gordon et al. (2011) found  
106 that the frequent occurrence of net upward aerosol flux was associated with decoupled canopy conditions where entrainment  
107 of particle-free air from above the canopy created a positive flux above the forest. On the other hand, Whitehead et al.  
108 (2010) found that the particle number concentration and submicron particle composition in the trunk space (i.e., below-  
109 canopy) and above-canopy environments showed minimal variation with height during daytime due to stronger turbulence  
110 and mixing conditions. In light of these limited studies, there is a need for additional measurements and data to inform the  
111 exchange of aerosols between the forest and the atmosphere.

112 Recent work from the Program for Research on Oxidants and PHotochemistry, Emissions and Transport (PROPHET)  
113 during the Atmospheric Measurements of Oxidants in Summer (AMOS) campaign in 2016 has indicated that flux of  
114 isoprene and monoterpenes at the canopy-atmosphere boundary represents over half of the net carbon flux, while oxygenated  
115 VOCs (OVOCs) constitute a majority of the species with detectable VOC fluxes (192 of the 236 species with identified  
116 molecular formulas). The authors report that the observed and modelled net carbon flux during the campaign was upward  
117 (canopy emission) during the campaign in 2016 (Millet et al., 2018). Vertical gradients of BVOCs in this mixed forest  
118 environment vary greatly depending on canopy vegetation height, primary emission versus secondary production, and  
119 diurnal variability (Alwe et al., 2019). Correlation analysis of VOC vertical gradients suggests that formic acid (HCOOH)  
120 originates from a secondary photochemical production. During the same campaign, distinct sample-to-sample variability in



121 the molecular-level aerosol composition (73 +/- 8%) was observed despite less variability in elemental composition of the  
122 bulk OA, indicating the chemical complexity of functionalized OA at the site (Ditto et al., 2018).

123 Here, measurements using an Aerodyne high-resolution time-of-flight aerosol mass spectrometer (HR-ToF-AMS) are  
124 used to characterize ambient aerosol above and below the canopy in a mixed, deciduous forest during the PROPHET-AMOS  
125 campaign in 2016. These measurements provide data for validation of forest canopy-atmosphere exchange models and  
126 allow an assessment of turbulent transport in the forest canopy and the resulting impacts on above- and below-canopy SOA  
127 composition and concentration. These data also could assist in the determination of whether or not SOA is forming within  
128 the forest canopy.

## 129 2 Methods

### 130 2.1 Site description

131 Measurements were made during the PROPHET-AMOS 2016 campaign from 1 July – 31 July 2016. The PROPHET  
132 site (45.55° N, 84.78° W) is situated in a temperate, mixed deciduous forest in the northern portion of Michigan's Lower  
133 Peninsula at the University of Michigan Biological Station (UMBS). The surrounding forest consists of aspens (60.9%),  
134 northern hardwoods (16.6%; maple, beech, birch, ash, and hemlocks), upland conifers (13.3%; white and red pines), non-  
135 forest cover types (7.6%; bracken ferns/grass/developed/road), and northern red oak (1.6%) (Cooper et al., 2001; Bergen and  
136 Dronova, 2007). The forests in this region are currently undergoing succession, where the dominant aspens have matured  
137 and are now being replaced by northern hardwoods and pines (Bergen and Dronova, 2007). It is expected that this new  
138 forest composition will shift BVOC emissions from an isoprene-dominated environment to one that is more influenced by  
139 monoterpenes (Toma and Bertman, 2012). The height of the forest canopy varies, but the mean canopy height is  
140 approximately 22.5 meters (VanReken et al., 2015). The site's physical layout and site meteorology have been described  
141 elsewhere (Carroll et al., 2001; Cooper et al., 2001). The PROPHET site features a 31-m scaffolding tower, allowing  
142 measurements to be made at variable heights within and above the vegetation canopy.

143 Due to the sparse surrounding population, the PROPHET site at UMBS has minimal local anthropogenic influences.  
144 The closest major urban centers include Detroit, Michigan (350 km to the southeast, population: 672,795), Milwaukee,  
145 Wisconsin (350 km to the southwest, population: 595,047), and Chicago, Illinois (450 km to the southwest, population:  
146 2,704,958) (Carroll et al., 2001). The closest nearby towns include Pellston, Michigan (5 km to the west, population: 828),  
147 Petoskey, Michigan (30 km to the southwest, population: 5,749), and Cheboygan, Michigan (30 km to the northeast,  
148 population: 4,726). Population totals are based on 2016 population estimates for cities and towns in the United States (US)  
149 from the US Census Bureau (US Census Bureau, 2018).

150 The mean temperature during the campaign was 20.6 +/- 4.6 °C (mean +/- one standard deviation), which is 3-4°C  
151 warmer than the mean temperature during the 2009 PROPHET-CABINEX campaign (16.9 °C) (VanReken et al., 2015).  
152 Temperature conditions during this study are consistent with mean summertime temperatures from studies in 2008 and 2010  
153 (Toma and Bertman, 2012) and with historical mean temperature data for the month of July from the Pellston Regional  
154 Airport (Figure S1 in the Supplemental Information (SI)). The mean relative humidity (RH) during the campaign was 73.8  
155 +/- 17.5% , which is similar to conditions during the CABINEX campaign (74.5 +/- 17.5%) (VanReken et al., 2015). Winds  
156 recorded at the top of the PROPHET tower originated mostly from the west, southwest, and northwest (as shown in Figure  
157 S2 in the SI). The historical average precipitation according to the National Atmospheric Deposition Program (NADP)  
158 National Trends Network for the month of July from 1979-2015 for UMBS is 69.0 +/- 37.8 mm. During the PROPHET-  
159 AMOS 2016 campaign, the total accumulated precipitation was 79.0 mm, indicating that precipitation at the site during the  
160 campaign was within one standard deviation of the historical July average (NADP, 2016).



## 161 2.2 Instrumentation and sampling

162 A summary of the trace-gas measurements, instrumentation, and meteorological parameters on board the University of  
163 Houston/Rice University Mobile Air Quality Laboratory (MAQL) are summarized in Table S1 of the SI. Details and  
164 operation of the MAQL have been described previously in the literature (Leong et al., 2017; Wallace et al., 2018). The  
165 MAQL was situated approximately 10 meters to the east of the PROPHET tower. A photograph of the MAQL in stationary  
166 sampling mode is shown in Figure S3 in the SI. Table S2 in the SI lists the measurements, measurement methods, and  
167 sampling heights of other participating institutions at PROPHET-AMOS 2016 during the campaign. Measurements are  
168 reported in local time (Eastern Daylight Time (EDT)) during the campaign.

### 169 2.2.1 Trace gases

170 Below-canopy trace gases including nitric oxide (NO), nitrogen dioxide (NO<sub>2</sub>), total reactive nitrogen (NO<sub>y</sub>), O<sub>3</sub>, carbon  
171 monoxide (CO), and sulfur dioxide (SO<sub>2</sub>) were measured from a common inlet on the sampling arm of the MAQL. Reported  
172 values of nitrogen oxides (NO<sub>x</sub>) represent the sum of NO and NO<sub>2</sub>, while reported values of NO<sub>y</sub> include NO<sub>x</sub> and its  
173 reservoir species. These measurements were taken at a height of 6 m above ground level.

### 174 2.2.2 HR-ToF-AMS

175 The HR-ToF-AMS (Aerodyne Research Inc., USA) was used to measure non-refractory submicron particulate matter  
176 (NR-PM<sub>1</sub>) from the MAQL; measured composition includes OA, SO<sub>4</sub>, nitrate (NO<sub>3</sub>), ammonium (NH<sub>4</sub>), and chloride (Cl).  
177 Detailed descriptions of the operation and principles of the HR-ToF-AMS have been provided elsewhere (DeCarlo et al.,  
178 2007). In brief, particles are sampled through a 100-micron critical orifice and are focused into a particle beam using an  
179 aerodynamic lens. After traversing a vacuum chamber, the particles in the beam impact onto a tungsten vaporizer heated to  
180 600°C. The vapors formed are ionized by electron impact ionization at 70 eV. The resulting ions are detected using a high-  
181 resolution time-of-flight mass spectrometer. The HR-ToF-AMS was operated in a high mass sensitivity mode, referred to as  
182 V-mode. Ionization efficiency (IE) calibrations were performed at the beginning and end of the campaign using  
183 monodisperse 300 nanometer NH<sub>4</sub>NO<sub>3</sub> particles. Gas-phase interferences were subtracted from the data based on the  
184 observed signal when ambient air was sampled through a filter. Filter zeros were run each day at varying times of day.

185 Sampling was performed from the raised 6-m inlet on the common sampling arm of the MAQL (below canopy) and  
186 from a 30-m inlet on the PROPHET tower (above canopy). Copper tubing was used for the sampling inlets, and each inlet  
187 was fitted with cyclones to remove particles larger than 2.5 microns in diameter. Prior to the HR-ToF-AMS critical orifice,  
188 air was sampled through a nafion dryer to dry the sample flow. A three-way valve was used to alternate HR-ToF-AMS  
189 sampling between the above- and below-canopy inlets at 10-minute intervals.

### 190 2.2.3 PTR-QiToF

191 Above-canopy mixing ratios and fluxes, along with in-canopy vertical gradients, were measured for a wide array of  
192 VOCs during PROPHET-AMOS 2016 by Proton Transfer Reaction-Quadrupole interface Time-Of-Flight mass spectrometry  
193 (PTR-QiToF). A detailed description of the sampling configuration, calibration and zeroing procedures, humidity  
194 corrections, and instrumental performance during the campaign is provided by Alwe et al. (2019) and Millet et al. (2018).  
195 Briefly, six identical 45-m inlet lines (0.5" OD/0.375" ID PFA, each heated to 50°C) were installed on the PROPHET tower  
196 to sample from 34 m, 21 m, 17 m, 13 m, 9 m, and 5 m above ground level. Sample flow was maintained at ~40 standard  
197 L/min (SLM) for the 34 m inlet line and at >5-10 SLM for the others. Each hour, 30 min was spent sampling from the 34 m  
198 inlet to quantify above-canopy VOC mixing ratios and fluxes. The remainder of each hour was spent characterizing in-  
199 canopy vertical gradients by sequentially sampling from the other inlets (for 5 min apiece) followed by a 5-min instrumental  
200 blank.



### 201 2.3 HR-ToF-AMS data and positive matrix factorization analysis

202 Data analysis for HR-ToF-AMS data was performed in Igor Pro v6.37 using the SQUIRREL v1.57 (SeQUential Igor  
203 data RetRiEval) and PIKA v1.16 (Peak Integration by Key Analysis) analysis toolkits. High-resolution mass spectral fitting  
204 was performed on HR-ToF-AMS V-mode data. Ratios such as the oxygen-to-carbon elemental ratio (O:C) and hydrogen-to-  
205 carbon elemental ratio (H:C) were determined according to the “improved-ambient” (IA) method (Canagaratna et al., 2015).  
206 The IA method uses specific ion fragments to correct for compositional biases, and this method has been shown to calculate  
207 accurately the elemental ratios of organic laboratory standards that are more representative of oxidized, ambient OA species  
208 (Canagaratna et al., 2015). The default values for relative IE were used for each of the following species: OA (1.4), SO<sub>4</sub>  
209 (1.2), NH<sub>4</sub> (4), NO<sub>3</sub> (1.1), and Chl (1.3), where values in parentheses refer to the ratio of the IE of the given species with  
210 respect to the value of IE of NO<sub>3</sub> obtained during routine IE calibrations using NH<sub>4</sub>NO<sub>3</sub>.

211 To account for the effects of aerosol composition on the transmission efficiency of aerosols to the detection region of the  
212 HR-ToF-AMS, a chemical composition-dependent (and therefore time-dependent) collection efficiency (CDCE) was applied  
213 to the HR-ToF-AMS data (Middlebrook et al., 2012), which led to an campaign average CDCE of 0.77 +/- 0.18. During the  
214 campaign, the HR-ToF-AMS time resolution was 40 seconds from 2 July 02:00 to 19 July 10:00 EDT, after which the HR-  
215 ToF-AMS time resolution was changed to 30 seconds between 22 July 11:00 and 31 July 15:00 EDT (due to instrumental  
216 changes after an HR-ToF-AMS power supply failure). Calculated detection limits of NR-PM<sub>1</sub> species are included in Table  
217 S3.

218 Positive matrix factorization (PMF) is a mathematical model in which measured data are decomposed into a  
219 combination of factors that have varying contributions throughout a time series. Here, the PMF model has been applied to  
220 HR-ToF-AMS data to retrieve OA factors that contain information regarding OA sources, chemical properties, and/or  
221 atmospheric processing (Jimenez et al., 2009; Ulbrich et al., 2009; Zhang et al., 2011). Subtypes of OA extracted from OA  
222 mass spectra using PMF often include (but are not limited to): more-oxidized oxygenated OA (MO-OOA), less-oxidized  
223 oxygenated OA (LO-OOA), hydrocarbon-like OA (HOA), biomass burning organic aerosol (BBOA), and cooking organic  
224 aerosol (COA) (Cubison et al., 2011; Jimenez et al., 2009; Mohr et al., 2012; Zhang et al., 2007, 2005). The OOA-related  
225 factors are generally considered to be associated with SOA, while subtypes such as HOA, BBOA, and COA are presumed to  
226 correspond to POA. Factors associated with isoprene-derived epoxydiol OA (IEPOX-OA) have also been identified using  
227 PMF using enhanced signals at m/z 82 in their OA mass spectra (Hu et al., 2015).

228 Factorization of HR-ToF-AMS data follows the matrix form:

$$229 \quad X = GF + E \quad (1)$$

230 where  $X$  is a  $m \times n$  matrix in which rows are the measured mass spectra at each time interval and columns are the time-  
231 varying signals of each sampled mass-to-charge ratio (m/z).  $G$  is a  $m \times p$  matrix in which rows are the concentration time  
232 series for a given factor, and the number of factors (columns) in the solution is represented by  $p$ .  $F$  is a  $p \times n$  matrix in  
233 which  $p$  rows are the mass spectral profiles for a given factor. Finally,  $E$  is a  $m \times n$  matrix and contains the residuals not fit  
234 by the model at each time interval and sampled m/z. Using a least-squares algorithm, the values of  $G$  and  $F$  are determined  
235 by minimizing  $E$  using a quality of fit parameter ( $Q$ ) defined as the squared sum of the scaled residuals:

$$236 \quad Q = \sum_{i=1}^m \sum_{j=1}^n \left( \frac{e_{ij}}{\sigma_{ij}} \right)^2 \quad (2)$$

237 where  $\sigma_{ij}$  is the estimated standard deviation of the points in the data matrix,  $X$ , and  $e_{ij}$  is an element in in the model residual  
238 matrix,  $E$ . Scaling in  $Q$  is calculated using reduced weights towards outliers, thus allowing for weighting of the input data  
239 by their level of measurement certainty (standard deviations in the data matrix,  $X$ ) (Paatero and Tapper, 1994; Ulbrich et al.,  
240 2009). The number of factors is generally unknown a priori and is determined based on the interpretation of PMF results.  
241 The selection of the number of factors can be aided using mathematical metrics, including  $Q/Q_{exp}$ , where  $Q_{exp}$  represents  
242 the degrees of freedom in the dataset ( $Q_{exp} = mn - p(m + n)$ ). As values of  $Q/Q_{exp}$  approach 1, the appropriate number  
243 of modeled factors is determined.



244 In this study, PMF is applied separately to the above- and below- canopy HR-ToF-AMS OA high-resolution mass  
245 spectra between  $m/z$  12 and  $m/z$  115 using the generic 64-bit PMF2 v4.2 algorithm running in robust mode with a model  
246 error set to zero (Paatero, 1997; Paatero and Tapper, 1994; Ulbrich et al., 2009). The default PMF2 convergence criteria  
247 were used. The PMF Evaluation Tool v2.08 (PET) in Igor Pro v6.37 was used to treat the OA mass spectra error matrix,  
248 evaluate PMF output, and examine model statistics (Ulbrich et al., 2009). Organic isotopes were excluded from PMF  
249 analysis because isotope signals are scaled from their parent ions rather than being measured directly. A minimum error  
250 threshold was applied to the error matrix where any error values falling below this threshold are replaced. Variables (time  
251 series of  $m/z$  values) with a signal-to-noise ratio (SNR) less than 0.2 were removed, and variables with a SNR less than 2  
252 were downweighted by a factor of 2. The error values for fragments such as  $O^+$ ,  $HO^+$ ,  $H_2O^+$ , and  $CO_2^+$  were also  
253 downweighted to avoid providing additional weight to the strong signal attributed to  $m/z$  44 in the default fragmentation  
254 table. To decrease the weight of each of these fragments, the error values for each of these fragment ions are all multiplied  
255 by a factor of 2 to appropriately downweight the  $m/z$  values related to  $m/z$  44. Additionally, the error of the  $CHO^+$  fragment  
256 was downweighted by multiplying the error value for this fragment by a factor of 4. Downweighting of  $CHO^+$  was  
257 performed because  $m/z$  29 is a combination of signals from the  $CHO^+$  ion ( $m/z$  29.0027) and a  $N_2$  isotope ion (j15NN,  $m/z$   
258 29.0032). The close proximity of the  $CHO^+$  and j15NN fragments ( $< 0.001$ ) using PIKA v1.16 likely causes the  $CHO^+$  error  
259 to be underestimated (Xu et al., 2015).

260 The optimal PMF solution for the OA data was determined by examining the following: (1) time series and mass spectra  
261 model residuals, (2) interpretability of factor diurnal variability, (3) correlations between factor time series and time series of  
262 external data, individual values, or tracers, (4) factor mass spectral characteristics, and (5) reductions in  $Q/Q_{exp}$ . The  
263 rotational ambiguity for each solution was explored by running PMF under a number of different FPEAK values, ranging  
264 from -1.0 to 1.0 in increments of 0.2. A change to the FPEAK parameter explores the different linear transformations (also  
265 referred to as “rotations”) of a given solution that result in identical fits to the data (Ulbrich et al., 2009). The robustness of  
266 each solution was evaluated by initializing the PMF model for a number of different starting points (or SEED values),  
267 ranging from 0 to 50 in increments of 1. In addition to the FPEAK and SEED analysis performed on the optimal PMF  
268 solution, the quantitative uncertainty of the solution is performed on the original  $m/z$  and time series data using  
269 bootstrapping analysis, where 100 PMF model runs are executed with replacement of the mass spectra. Variations ( $1\sigma$ ) of  
270 the average factor mass spectra at each  $m/z$  and average factor time series are used to assess the robustness of the optimal  
271 PMF solution (Ulbrich et al., 2009).

272 The results of the separate PMF analyses on above- and below-canopy OA are included in the SI. For the above-canopy  
273 OA data, a summary of the PMF factor selection (Table S4), factor time series correlations with external data (Table S5),  
274 factor mass spectra correlations with reference mass spectra (Table S6), time series of PMF model residuals (Figure S4), and  
275 mass spectra and time series for possible two- to five-factor PMF solutions (Figure S5 - Figure S8) are shown in the SI.  
276 VOCs measured above-canopy via PTR-QiToF at the top of the PROPHET tower are defined in Table S7, and factor time  
277 series correlations with the time series of these VOCs are shown in Table S8. PMF diagnostics, such as the mass spectra and  
278 time series correlation amongst factors (Figure S9), FPEAK and SEED diagnostic plots (Figure S10), results of the FPEAK  
279 analysis (Table S9), model residual diagnostic plots (Figure S11), and results from bootstrapping analysis (Figure S12) are  
280 shown in the SI. Finally, Figure S13 displays the time series and high-resolution mass spectra of the optimal solution for the  
281 above-canopy OA dataset.

282 For the below-canopy OA data, a summary of the PMF factor selection (Table S10), factor time series correlations with  
283 external data (Table S11), factor mass spectra correlations with reference mass spectra (Table S12), mass spectra and time  
284 series of possible two- to five-factor PMF solutions (Figure S14 - Figure S17), factor time series correlations with VOCs  
285 measured via PTR-QiToF at the 34-m inlet on the PROPHET tower (Table S13), mass spectra and time series correlations  
286 amongst factors (Figure S18), FPEAK and SEED diagnostic plots (Figure S19), results from FPEAK analysis (Table S14  
287 and Table S15), model residual diagnostic plots (Figure S20), and results from bootstrapping analysis (Figure S21) are  
288 shown in the SI. Finally, the time series and high-resolution mass spectra of the optimal three-factor solution for below-  
289 canopy OA are shown in Figure S22.



## 290 2.4 HYSPLIT backward trajectory analysis

### 291 2.4.1 Trajectory cluster analysis

292 Backward-trajectories are used in this study to determine the origin of air masses arriving at the field site using the  
293 Hybrid Single-Particle Lagrangian Integrated Trajectory (HYSPLIT) model (Draxler and Hess, 1998; Stein et al., 2015).  
294 Meteorological data from the US Eta data assimilation system archive at 40-km spatial resolution (EDAS40) are used for  
295 HYSPLIT trajectory calculations. The EDAS40 data output is constructed using forecasted data from the Eta model, which  
296 utilizes observations from surface, aircraft, and satellite data to predict meteorological parameters such as pressure, wind  
297 speed, and wind direction (Cooper et al., 2001).

298 In order to assess the influence of air mass histories on aerosols at each site, a cluster analysis was performed on  
299 backward trajectories using MeteoInfo v1.4.9R2 and the TrajStat v1.4.4R8 package (Wang, 2014; Wang et al., 2009). The  
300 angle distance clustering type is used in this study and calculates the angular distance between two backward trajectories as  
301 seen from the site, using methods outlined in Sirois and Bottenheim (1995). The number of suitable clusters is chosen based  
302 on the slope of the percentage change in total spatial variation versus number of clusters and a visual inspection of the mean  
303 trajectories of the cluster numbers.

### 304 2.4.2 Weighted potential source contribution function (WPSCF) analysis

305 In addition to a backward-trajectory cluster analysis performed for bulk aerosol properties and gas-phase species, two-  
306 day HYSPLIT backward-trajectories initiated from the PROPHET site at 500 m above ground level are used in a weighted  
307 potential source contribution function (WPSCF) analysis for OA factors. WPSCF analysis is performed in MeteoInfo  
308 v1.4.9R2 using the TrajStat v1.4.4R8 package and results are plotted using ESRI's ArcMap v10.1 (Wang, 2014; Wang et al.,  
309 2009). Similar PSCF analyses using backward-trajectories have been performed previously using aerosol properties (Bondy  
310 et al., 2017; Chang et al., 2017; Polissar, 1999; Schulze et al., 2018).

311 The number of backward-trajectory endpoints falling within a given grid cell with coordinates  $(i, j)$  is defined as  $n_{ij}$ .  
312 The number of instances in which backward-trajectories ending at a given grid cell have a value (i.e., OA factor mass  
313 concentration) higher than an arbitrarily set criterion value is defined as  $m_{ij}$ . The PSCF value for a cell at location  $(i, j)$  is  
314 then defined as follows:

$$315 \text{PSCF}_{ij} = \frac{m_{ij}}{n_{ij}} \quad (3)$$

316 When calculating values of PSCF, some grid cells will contain only a small number of backward-trajectory endpoints. In  
317 order to reduce the high uncertainties related to a limited number of endpoints falling within a grid cell in PSCF analysis, a  
318 weighting function is applied to the trajectory numbers following the methods of Polissar et al. (2001):

$$319 W_{ij} = \begin{cases} 1.00 & 80 < n_{ij} \\ 0.70 & 20 < n_{ij} \leq 80 \\ 0.42 & 10 < n_{ij} \leq 20 \\ 0.05 & n_{ij} \leq 10 \end{cases} \quad (4)$$

320 In this study, the domain of analysis is set to the geographical extents of the two-day HYSPLIT backward trajectories  
321 initiated from the PROPHET site. A grid cell size of  $0.5^\circ$  by  $0.5^\circ$  is used. Median values of the OA factors are used as the  
322 arbitrary criterion values. Overall, the WPSCF analysis allows for an identification of potential source areas, where higher  
323 WPSCF values within a region indicate a higher likelihood that this region results in observed values higher than the  
324 criterion values.





## 325 2.5 Sonic anemometer data-processing

326 Turbulence measurements during the campaign were obtained from five sonic anemometers installed on the PROPHET  
327 tower at the following measurement heights: 34m (CSAT 3B, Campbell Scientific Inc.), 29m (81000, RM Young), 21m  
328 (CSAT 3, Campbell Scientific Inc.), 13m (CSAT 3, Campbell Scientific Inc.), and 5m (CSAT 3, Campbell Scientific Inc.).  
329 The sonic anemometer at 34 m was operated continuously during the campaign while data are only available from the lower  
330 heights from July 9<sup>th</sup>, 2016 – July 29<sup>th</sup>, 2016. High-frequency data are de-spiked (data points outside of 3.5-standard  
331 deviations are removed) and then separated into 30-minute windows to apply a tilt correction such that the x-axis is rotated  
332 into the direction of the mean wind velocity (Foken, 2008). Reynolds decomposition is then applied to the three-dimensional  
333 wind components ( $u, v, w$ ), so each variable (e.g.,  $u$ ) is separated into its mean ( $\bar{u}$ ) and fluctuating component ( $u'$ ). The  
334 friction velocity,  $u^*$ , is defined then as

$$335 u^*{}^2 = -\overline{u'w'} \quad (5)$$

336 Any 30-minute periods that experienced rain (as measured by the rain-gauge at the UMBS AmeriFlux tower), weak winds  
337 (winds less than  $0.5 \text{ m s}^{-1}$  at the top sonic anemometer), or wind directed through the tower were excluded due to potential  
338 interference.

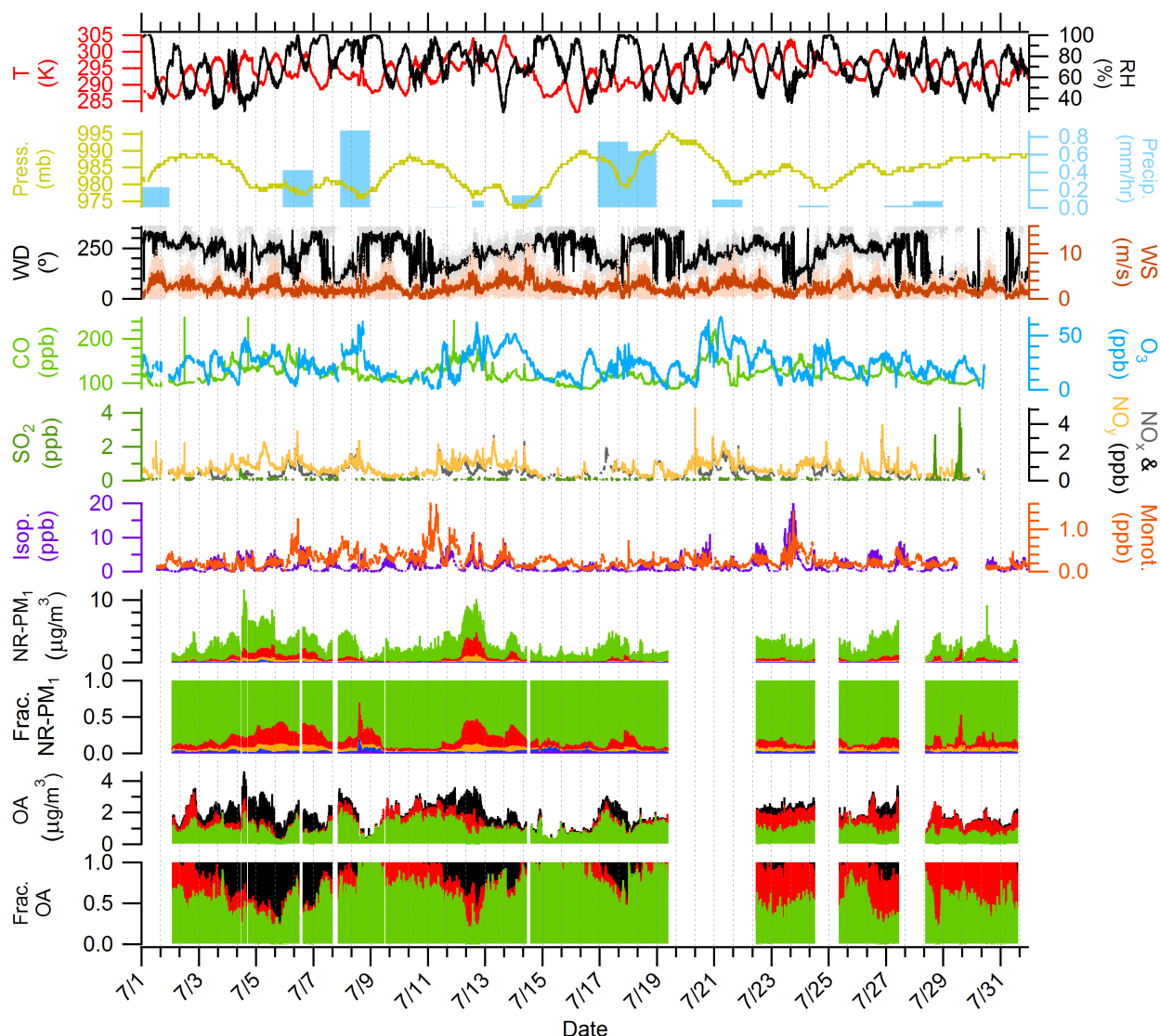
## 339 3 Results and discussion

### 340 3.1 Backward-trajectory cluster analysis

341 Two-day backward trajectories are initiated from the PROPHET site and calculated at one-hour intervals from the  
342 beginning to the end of the campaign (1 July 00:00 – 31 July 21:00 EDT) at 500 meters above ground level, an elevation  
343 selected to be within the boundary layer during the day and to avoid trajectory interaction with the surface. A total of 742  
344 two-day backward-trajectories are calculated over the course of the campaign. Cluster analysis resulted in three directional  
345 clusters: southerly (299 of 742), northeasterly (192 of 742), and northwesterly (251 of 742) (as shown in Figure S23 in the SI  
346 as Cluster 1, 2, and 3 respectively). Further description of cluster number selection is discussed in Figure S24 in the SI.  
347 Similar to the air mass history analyses at the PROPHET site in Cooper et al. (2001) and VanReken et al. (2015), eight-hour  
348 transitional periods between backward-trajectory classifications were removed from analysis because it is likely that the  
349 chemical species from these different air masses are mixed. In total, transitional periods composed 22% of the total number  
350 of backward-trajectories (165 of 742 total), and the remaining 577 are used for further analysis. Mean values of  
351 anthropogenically-influenced species such as  $\text{SO}_4$  and benzene were not statistically significantly different ( $p < 0.01$ )  
352 between trajectories from northeasterly and northwesterly clusters, so trajectories from these two clusters are grouped to  
353 represent a “northerly” air mass type. During the PROPHET-AMOS study, northerly transport occurred during 60% of the  
354 study period (341 of 577), while southerly transport occurred 40% of the time (236 of 577). This type of air-mass  
355 classification is consistent with previous summertime studies at the PROPHET site where northerly transport occurred 44%  
356 (1998), 60% (2009), and 57% (2014) of the time and southerly transport occurred 24% (1998), 29% (2009), and 43% (2014)  
357 of the time (Cooper et al., 2001; Gunsch et al., 2017; VanReken et al., 2015).

### 358 3.2 Non-refractory submicron time series and bulk chemical composition

359 Figure 1 shows the time series of the mass concentrations of OA,  $\text{SO}_4$ ,  $\text{NH}_4$ ,  $\text{NO}_3$ , and Chl as measured by the HR-ToF-  
360 AMS. Mass concentrations plotted in Figure 1 represent time series data from both the above- and below-canopy sampling  
361 inlets. The average total NR- $\text{PM}_{10}$  (sum of mass concentrations of OA,  $\text{SO}_4$ ,  $\text{NH}_4$ ,  $\text{NO}_3$ , and Chl) is  $2.3 \pm 1.5 \mu\text{g m}^{-3}$ . High  
362 NR- $\text{PM}_{10}$  concentration episodes (7/3-7/7 and 7/11-7/14) are strongly influenced by southerly air masses advecting



363  
 364 **Figure 1: Overview of time series of the following from top to bottom: temperature (T) and RH; pressure (Press.)**  
 365 **and precipitation (Precip.); wind direction (WD) and wind speed (WS); CO and O<sub>3</sub>; SO<sub>2</sub>, NO<sub>x</sub>, and NO<sub>y</sub>; isoprene**  
 366 **(Isop.) and total monoterpenes (Monot.); particulate OA (green), NO<sub>3</sub> (blue), SO<sub>4</sub> (red), NH<sub>4</sub> (orange), and Chl**  
 367 **(purple); fraction of species to total NR-PM<sub>1</sub>, OA factors derived from PMF, and fractional contribution of OA**  
 368 **factors to total OA. OA factors are colored as follows: MO-OOA (black), IEPOX-OA (red), and 91Fac (green).**  
 369 **Precipitation data are provided from the NADP site in Cheboygan County, MI. Trace gas data (CO, O<sub>3</sub>, SO<sub>2</sub>, NO<sub>x</sub>,**  
 370 **and NO<sub>y</sub>) are measured from the 6-m inlet on the MAQL. Meteorological data (T, RH, Press., WD, and WS) and**  
 371 **VOC data (Isop. and Monot.) are measured from the 34-m inlet on the PROPHET tower.**

372  
 373 to the site, as confirmed by the HYSPLIT backward-trajectory clusters shown in Figure S23 in the SI. Northerly backward-  
 374 trajectories originated over clean, remote areas in Canada, while southerly backward-trajectories originated over more  
 375 anthropogenically influenced areas. OA is the dominant NR-PM<sub>1</sub> component over the entire campaign, representing  
 376 approximately 84.2% of the NR-PM<sub>1</sub> mass. SO<sub>4</sub> contributes the second highest average mass fraction to NR-PM<sub>1</sub> (10.7%)



377 followed by  $\text{NH}_4$  (3.1%),  $\text{NO}_3$  (1.6%), and Chl (0.4%). During periods of northerly flow, OA represents 89.5% of the  
378 average NR- $\text{PM}_{10}$  mass, while  $\text{SO}_4$ ,  $\text{NH}_4$ ,  $\text{NO}_3$  and Chl represent 6.9%, 1.9%, 1.3%, and 0.4%, respectively. Periods of  
379 southerly flow decrease the relative contribution of OA to 75.5% and Chl to 0.3% while increasing the relative contribution  
380 of  $\text{SO}_4$  to 16.8%,  $\text{NH}_4$  to 5.6%, and  $\text{NO}_3$  to 1.3%. The increased fractional contribution of OA during periods of northerly-  
381 originating air is consistent with results from VanReken et al. (2015), who found that water-soluble organics dominated  
382 aerosol mass during periods of “clean” northerly flow at the PROPHET site. Sheesley et al. (2004) also found the aerosol  
383 organic carbon composition at a remote site in the upper peninsula of Michigan (approximately 100 miles from the  
384 PROPHET site) was greatly influenced by the source region of the air parcel. This study found that both stagnant and  
385 northerly air parcels contained higher concentrations of pinonic acid and limited amounts of primary emission tracer  
386 compounds, while anthropogenically influenced air parcels from the south and northwest contained higher concentrations of  
387 aromatic and aliphatic dicarboxylic acids.

388 Diurnal plots for OA,  $\text{SO}_4$ ,  $\text{NH}_4$ ,  $\text{NO}_3$ , O:C, and H:C are shown in Figure S25 in the SI. The diurnal profiles of OA,  
389  $\text{SO}_4$ , and  $\text{NH}_4$  are all relatively flat and do not have a clear diurnal trend. The lack of clear diurnal variations for  $\text{SO}_4$  is  
390 consistent with regional transport as the source of  $\text{SO}_4$  during this campaign. The diurnal variations of  $\text{NO}_3$  show increases  
391 in the morning, with a maximum around approximately 10:00 local time, and lower concentrations in the afternoon.

392 Using the backward-trajectory clustering results described in Section 3.1, mean values of NR- $\text{PM}_{10}$ , NR- $\text{PM}_{10}$  species, OA  
393 elemental ratios, meteorological parameters, and trace gases for the entire campaign, northerly, and southerly backward-  
394 trajectory clusters are shown in Table 1. Overall, relative to northerly air masses, southerly air masses were found to be  
395 warmer ( $\sim 2$  °C), more humid ( $\sim 5\%$ ), and associated with higher concentrations of  $\text{NO}_x$ ,  $\text{NO}_y$ ,  $\text{O}_3$ , and benzene. Furthermore,  
396 on average, southerly air masses had higher concentrations of NR- $\text{PM}_{10}$ , OA,  $\text{SO}_4$ ,  $\text{NH}_4$ , and  $\text{NO}_3$ . Higher levels of OA  
397 oxidation (8% difference) based on O:C are also observed during periods of southerly flow (O:C = 0.69 versus 0.75 for  
398 northerly versus southerly flow, respectively). An additional metric of oxidation, the oxidation state of carbon (OSc),  
399 indicates that the degree of oxidation is higher during periods of southerly flow (OSc = -0.12 versus 0.06 for northerly versus  
400 southerly flow, respectively, where  $\text{OSc} = 2 * \text{O:C} - \text{H:C}$ ) (Kroll et al., 2011). The factor of 5 differences between northerly  
401 and southerly  $\text{SO}_4$  is consistent with the increased influence of  $\text{SO}_2$  point sources from electric-generating units south of the  
402 site in Ohio, Indiana, and Illinois. Overall, these observations demonstrate that anthropogenic influence from southerly flow  
403 directly affects NR- $\text{PM}_{10}$  mass concentrations, NR- $\text{PM}_{10}$  composition, the degree of OA oxidation, and trace gas mixing ratios  
404 at this site. Results are in agreement with VanReken et al. (2015), where southerly air masses or those “anthropogenically  
405 impacted” were found to contain higher aerosol loadings (in terms of aerosol volume, particle number, and median particle  
406 diameter) and hygroscopicity, along with increased trace gases abundances, as compared to northerly air masses or “clean”  
407 regimes.

408 Oxygen-containing ion families ( $\text{C}_x\text{H}_y\text{O}_{z\geq 1}^+$ ) represent over 50% of the campaign-averaged OA high-resolution mass  
409 spectrum, and this high degree of oxygenation is reflected in an average O:C ratio of 0.71  $\pm$  0.08 and an average H:C ratio  
410 of 1.49  $\pm$  0.06. A distinct peak at  $m/z$  44 in the average mass spectrum accounts for 14.1% of the total OA. The peak at  
411  $m/z$  44 is mainly composed of the  $\text{CO}_2^+$  ion (96.0% of  $m/z$  44). The ratio of  $m/z$  44 to the total signal in the organic mass  
412 spectrum ( $f_{44}$ ), a surrogate for O:C and an indicator for photochemical aging, in this study is 0.14. Together with the average  
413 O:C ratio (0.71) observed in this study, these values are consistent with OOA observed across AMS datasets (Jimenez et al.,  
414 2009; Ng et al., 2010). Other prominent ions in the campaign-averaged high-resolution mass spectrum include  $m/z$  55, 82,  
415 and 91. Fragments at  $m/z$  55 represent 2.4% of the total OA, and are representative of both oxygenated and hydrocarbon  
416 fragments, such as  $\text{C}_3\text{H}_3\text{O}^+$  (50.2% of  $m/z$  55) and  $\text{C}_4\text{H}_7^+$  (42.9% of  $m/z$  55). The possible OA sources leading to increased  
417 signal at  $m/z$  82 (0.46% of total OA) and 91 (0.62% of total OA) will be discussed in the following section. Figure S25 in  
418 the SI shows the diurnal variations of O:C and H:C, indicating relatively stable diurnal cycles. Increases in H:C are observed  
419 starting at 9:00 before reaching a maximum at midday (13:00) followed by a slow decrease between the hours of 13:00 and  
420 20:00, while an opposite pattern is observed for mean values of O:C.

421



422 **Table 1: Campaign-averaged values (+/- one standard deviation from the mean) of mass concentrations of NR-PM<sub>1</sub>, VOC and**  
 423 **trace gas mixing ratios, and meteorological parameters, as well as hourly-averaged values associated with northerly and southerly**  
 424 **backward-trajectory clusters. Northerly and southerly air masses are defined in Section 3.1 using a cluster analysis of HYSPLIT**  
 425 **two-day backward trajectories.**

Parameter	Campaign	Northerly	Southerly
NR-PM <sub>1</sub> (µg m <sup>-3</sup> )	2.3 ± 1.5	1.8 ± 0.7	3.6 ± 2.0
OA (µg m <sup>-3</sup> )	1.9 ± 1.0	1.6 ± 0.6	2.6 ± 1.3
SO <sub>4</sub> (µg m <sup>-3</sup> )	0.3 ± 0.4	0.1 ± 0.1	0.7 ± 0.6
NH <sub>4</sub> (µg m <sup>-3</sup> )	0.1 ± 0.1	0.04 ± 0.04	0.2 ± 0.2
NO <sub>3</sub> (µg m <sup>-3</sup> )	0.04 ± 0.03	0.02 ± 0.01	0.06 ± 0.05
Chl (µg m <sup>-3</sup> )	0.01 ± 0.00	0.01 ± 0.00	0.01 ± 0.00
O:C	0.7 ± 0.1	0.7 ± 0.1	0.8 ± 0.1
H:C	1.5 ± 0.1	1.5 ± 0.0	1.4 ± 0.00
OSc	-0.1 ± 0.2	-0.1 ± 0.1	0.1 ± 0.2
Isoprene (ppb) <sup>a, b</sup>	1.6 ± 1.9	1.5 ± 1.5	1.8 ± 1.5
Monoterpenes (ppb) <sup>a, b</sup>	0.3 ± 0.2	0.2 ± 0.1	0.2 ± 0.2
Benzene (ppb) <sup>a</sup>	0.04 ± 0.02	0.03 ± 0.01	0.05 ± 0.02
NO (ppt) <sup>c</sup>	24.1 ± 36.4	21.5 ± 16.2	29.7 ± 29.5
NO <sub>2</sub> (ppt) <sup>c</sup>	593.0 ± 445.8	369.4 ± 257.7	872.0 ± 478.6
NO <sub>y</sub> (ppt) <sup>c</sup>	934.5 ± 490.0	610.5 ± 271.8	1283.9 ± 412.6
O <sub>3</sub> (ppb) <sup>c</sup>	24.1 ± 11.9	20.1 ± 8.3	30.5 ± 13.2
CO (ppt) <sup>c</sup>	120.6 ± 21.5	109.6 ± 12.6	134.7 ± 21.7
SO <sub>2</sub> (ppb) <sup>b, c</sup>	31.3 ± 174.2	45.0 ± 212.0	23.1 ± 64.2
Temperature (°C) <sup>c</sup>	20.6 ± 4.6	20.3 ± 4.5	22.4 ± 4.5
Relative Humidity (%) <sup>c</sup>	73.8 ± 17.3	68.6 ± 17.0	73.5 ± 17.6

426 <sup>a</sup> VOC measurements using University of Minnesota's PTR-QiToF from the 34-m inlet on the PROPHET tower.

427 <sup>b</sup> Table entries where the differences between the northerly and southerly backward-trajectories mean values are not  
 428 statistically significant ( $p < 0.01$ ) using a two-sample t-test.

429 <sup>c</sup> Trace gas and meteorological parameters measured from onboard the MAQL.

430

### 431 3.3 Organic aerosol source apportionment

432 A three-factor solution is obtained for both the above-canopy inlet at 30 meters above the UMBS forest floor (A-MO-  
 433 OOA, A-IEPOX-OA, A-91Fac) and the below-canopy inlet at 6 meters within the UMBS canopy (B-MO-OOA, B-IEPOX-  
 434 OA, and B-91Fac). The addition of more factors to the PMF solution beyond three factors resulted in less physically  
 435 meaningful and interpretable factors. Thus, the three-factor solution is considered the optimal solution for the above- and  
 436 below-canopy OA datasets. In this study, seed = 0 was chosen for both PMF solutions as there was minimal variation in  
 437  $Q/Q_{exp}$  across the 50 seeds. Solutions at FPEAK = 0 were chosen because solutions at other FPEAK values did not present  
 438 improved correlations between factors and reference mass spectra.

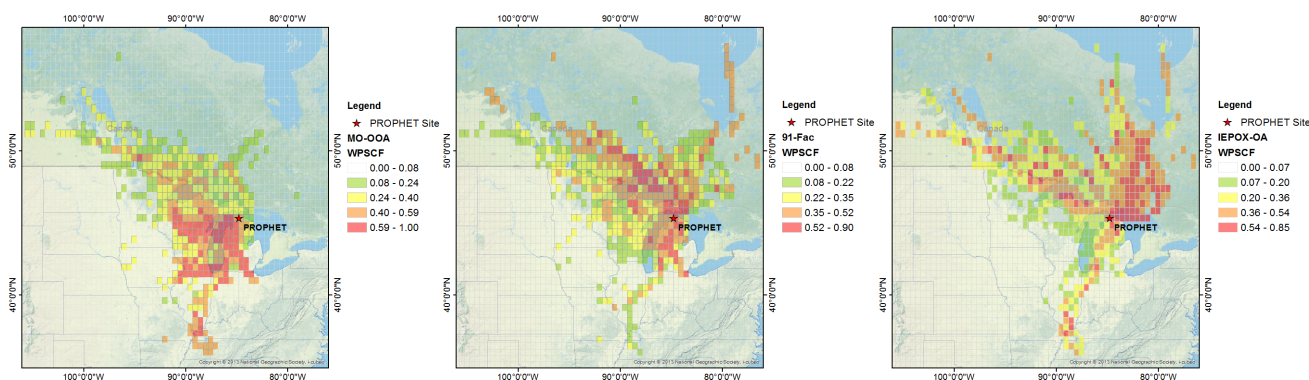
439 Time series of mass concentrations and time series of fractional contributions to total OA are shown in Figure 1. The  
 440 O:C ratio of each of the OA factors are as follows: 0.65 (IEPOX-OA), 0.71 (91Fac), and 0.89-0.90 (MO-OOA), all of which  
 441 indicate the high degree of oxygenation in each of the factors. For the above-canopy PMF solution, 91Fac makes the largest  
 442 contribution to the total OA (43.8%), followed by IEPOX-OA (32.8%) and MO-OOA (23.4%). For the below-canopy PMF



443 solution, 91Fac also makes the largest contribution to the total OA (42.5%), followed by IEPOX-OA (34.0%) and MO-OOA  
444 (23.5%). Details on the chemical composition, mass spectral characteristics and diurnal profiles of each factor are discussed  
445 further in the SI.

446 Hourly averages of the above-canopy OA factors are paired with hourly two-day backward-trajectories for WPSCF  
447 analysis. Results from WPSCF analysis using above-canopy OA data (Figure 2) indicate that A-MO-OOA predominantly  
448 originates from southerly air masses, as supported by external measurements data such as benzene, OVOCs, carbonyls, and  
449 SO<sub>4</sub>. Air masses that originate from the south pass over the large urban centers of Chicago, Milwaukee, and Detroit. This  
450 further supports the aged, transported nature and anthropogenic influences of the observed A-MO-OOA at this site. In  
451 contrast, no strong indication of a distinct source region is observed for 91Fac. This could suggest a more localized source  
452 of 91Fac in relation to the site. Combining these WPSCF results with correlations of 91Fac with VOC masses corresponding  
453 to monoterpene oxidation suggests that 91Fac is sourced from local biogenic, monoterpene-oxidation related chemistry (Xu  
454 et al., 2018). Finally, WPSCF results for A-IEPOX-OA indicate that this OA factor coincides with more northerly airflow  
455 with some contributions from northwesterly flow. These northerly source regions driving A-IEPOX-OA correspond to more  
456 rural, less anthropogenically influenced locations in Canada. Interestingly, an instance of high WPSCF values for A-  
457 IEPOX-OA and A-MO-OOA can be traced back to areas near the southeastern tip of Missouri and western Tennessee,  
458 implying long-range transport of these OA factors. Backward-trajectories associated with this instance of high WPSCF  
459 values for IEPOX-OA pass over areas in the high isoprene-emitting region in the Ozarks of southern Missouri, which is  
460 commonly referred to as the “isoprene volcano” (Carlton and Baker, 2011; Wiedinmyer et al., 2005). The median mass  
461 concentrations of above-canopy OA factors used as the criterion values for the WPSCF method were A-MO-OOA: 0.31  $\mu\text{g m}^{-3}$ ,  
462 A-91Fac: 0.68  $\mu\text{g m}^{-3}$ , and A-IEPOX-OA: 0.58  $\mu\text{g m}^{-3}$ . Overall, WPSCF analysis indicates that transport from southerly  
463 flow (A-MO-OOA), local sources (A-91Fac), and transport from northerly flow (A-IEPOX-OA) are related to the OA  
464 factors observed at this site.

465



466

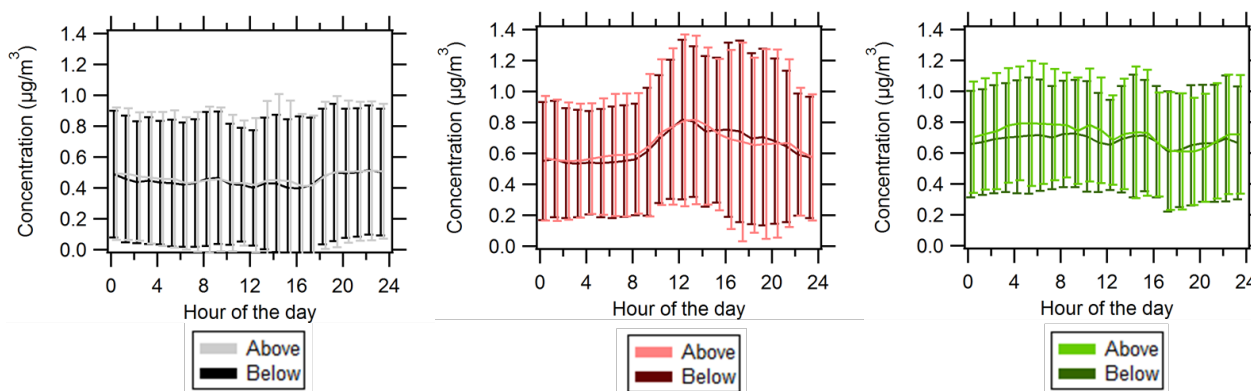
467 **Figure 2: WPSCF backward-trajectory analysis maps for the following hourly-averaged OA factors from left to right: above-**  
468 **canopy MO-OOA, above-canopy 91Fac and above-canopy IEPOX-OA. The geographical location of the PROPHECT site is**  
469 **represented by a red star. WPSCF analysis is performed using HYSPLIT two-day backward trajectories, a grid cell size of 0.5° by**  
470 **0.5°, and the geographical domain of the extents of the two-day backward trajectories. Median mass concentrations of above-**  
471 **canopy OA factors (A-MO-OOA: 0.31  $\mu\text{g m}^{-3}$ , A-91Fac: 0.68  $\mu\text{g m}^{-3}$ , and A-IEPOX-OA: 0.58  $\mu\text{g m}^{-3}$ ) are used as the criterion**  
472 **WPSCF values. Color scales correspond to probability of source regions for each respective OA factor, and it should be noted that**  
473 **the range and gradation of the color scale changes between each plot.**

474

475 Overall, PMF analysis for both sampling inlets at the site indicates that the OA is a combination of MO-OOA, 91Fac,  
476 and IEPOX-OA. The dominant OA factor is 91Fac, and during periods of southerly flow MO-OOA contributes relatively  
477 more (time series of the fractional contributions to total OA shown from both inlets is shown in Figure 1 and is also shown  
478 separately for each inlet in Figure S13 and Figure S22 in the SI). On average, source apportionment results indicate that the



479 OA at both inlets generally had similar average fractional OA contributions and degrees of oxidation. Diurnal profiles for  
480 above- and below-canopy OA are shown in Figure 3 and indicate that diurnal profiles and variations are similar between the  
481 two inlets for each OA factor. It is worth noting the diurnal pattern of the IEPOX-OA factor, likely indicating a relatively  
482 small influence of local isoprene emissions.  
483



484  
485 **Figure 3: Diurnal profiles of (left) MO-OOA, (middle) IEPOX-OA, and (right) 91Fac where solid lines represent average values**  
486 **and whiskers represent one standard deviation from the mean. Darker colors represent below-canopy OA (B-MO-OOA, B-**  
487 **IEPOX-OA, B-91Fac) while lighter colors represent above-canopy OA (A-MO-OOA, A-IEPOX-OA, A-91Fac). Data for below-**  
488 **canopy OA factors have been offset by 15 minutes simply to aid plot interpretation.**

489  
490 **3.4 Vertical characterization of above- and below-canopy NR-PM<sub>1</sub> and OA factors**

#### 491 3.4.1 Similarity between above- and below-canopy environments

492 Mean values of NR-PM<sub>1</sub>, NR-PM<sub>1</sub> species, OA elemental ratios, meteorological parameters, VOCs, and trace gases from  
493 the above- and below-canopy inlets are summarized in Table 2. Each of the mean values for the parameters listed in Table 2  
494 are within one standard deviation of each other for the below- and above-canopy sampling heights. However, results from  
495 Wilcoxon rank-sum tests indicate that the medians for a majority of the above- and below-canopy parameters are  
496 significantly different ( $p = 0.05$ ). To provide a comparison of the two inlets on the same time scale, scatter plots of 30-  
497 minute averaged values are shown in Figure 4 for OA factors, total OA, SO<sub>4</sub>, and O:C. For reference, a 1:1 line is shown on  
498 each scatter plot. Values falling within one standard deviation are similar between above and below canopy, while values  
499 deviating farther from the 1:1 line indicate values in which the above- or below-canopy environment had differing  
500 concentrations. Figure 4 illustrates that mass concentrations of OA factors, total OA, and SO<sub>4</sub> were similar over a majority  
501 of the campaign and suggests that the above- and below-canopy environments were generally coupled from a PM  
502 perspective. It also appears that total OA, MO-OOA, IEPOX-OA, and 91Fac show increases above canopy relative to below  
503 canopy at the highest end of the range of the measurements.

504 Results from a recent study from the PROPHET-AMOS 2016 campaign by Millet et al. (2018) indicate that flux of  
505 isoprene and monoterpenes at the canopy-atmosphere boundary represents over half of the net carbon flux, while OVOCs  
506 constitute a majority of the species with detectable VOC fluxes. Overall, the authors report that the observed and modeled  
507 net carbon flux during the campaign was upward (canopy emission) during the campaign in 2016. Additionally, in-canopy  
508 gradients of directly emitted BVOCs, such as isoprene and monoterpenes, indicate patterns that are consistent with their  
509 respective temperature, light, and physical emission dependencies (higher concentrations in-canopy for isoprene and higher  
510 in the lower canopy for monoterpenes). On the other hand, in-canopy gradients of secondary products from BVOC  
511 oxidation, such as acetic acid and glycoaldehyde, indicate patterns consistent with net nighttime uptake and a weak peak



512  
 513 **Table 2: Campaign-averaged values (+/- one standard deviation) of mass concentrations of NR-PM<sub>1</sub>, VOC and trace gas mixing**  
 514 **ratios, and meteorological parameters above and below the canopy.**

Parameter <sup>a, b</sup>	Above	Below
NR-PM <sub>1</sub> (μg m <sup>-3</sup> )	2.4 ± 1.6	2.3 ± 1.5
OA (μg m <sup>-3</sup> )	1.9 ± 1.0	1.8 ± 1.0
SO <sub>4</sub> (μg m <sup>-3</sup> )	0.3 ± 0.5	0.3 ± 0.4
NH <sub>4</sub> (μg m <sup>-3</sup> )	0.1 ± 0.2	0.1 ± 0.2
NO <sub>3</sub> (μg m <sup>-3</sup> )	0.04 ± 0.04	0.04 ± 0.03
Chl (μg m <sup>-3</sup> )	0.01 ± 0.00	0.01 ± 0.00
O:C	0.7 ± 0.1	0.7 ± 0.1
H:C <sup>c</sup>	1.5 ± 0.1	1.5 ± 0.1
OSc	0.0 ± 0.2	-0.1 ± 0.2
Isoprene (ppb)	1.6 ± 1.9	1.8 ± 2.2
Monoterpenes (ppb)	0.3 ± 0.2	0.3 ± 0.3
Benzene (ppb)	0.04 ± 0.02	0.04 ± 0.02
NO (ppt)	36.0 ± 56.9	24.1 ± 36.4
NO <sub>2</sub> (ppt)	564.8 ± 393.2	593.0 ± 448.8
O <sub>3</sub> (ppb)	32.2 ± 12.2	24.1 ± 11.9
Temperature (°C) <sup>c</sup>	20.7 ± 4.1	20.6 ± 4.6
Relative Humidity (%)	71.5 ± 17.3	73.8 ± 17.3

515 <sup>a</sup> Summary statistics for NR-PM<sub>1</sub> measurements were calculated using 5-minute averaged data, VOC measurements using 1-  
 516 minute averaged data (University of Minnesota's PTR-QiToF 5-m inlet and 34-m inlet), NO<sub>x</sub> above-canopy measurements  
 517 using 5-minute averaged data (University of Toronto), NO<sub>x</sub> and O<sub>3</sub> below-canopy measurements using 5-minute averaged  
 518 data (MAQL), and O<sub>3</sub> 1-minute averaged data (CU-Boulder's 27-m inlet on the AmeriFlux Tower).

519 <sup>b</sup> Percent of data below detection limit for NR-PM<sub>1</sub>: NH<sub>4</sub> (4% / 4%) and Chl (59% / 63%), VOCs: isoprene (30% / 30%),  
 520 monoterpenes (56% / 36%), benzene (100% / 100%), and NO (37% / 22%), where percentages are shown for above- and  
 521 below-canopy data, respectively. Unless otherwise stated, the percentage below detection limit for all other parameters is  
 522 0%.

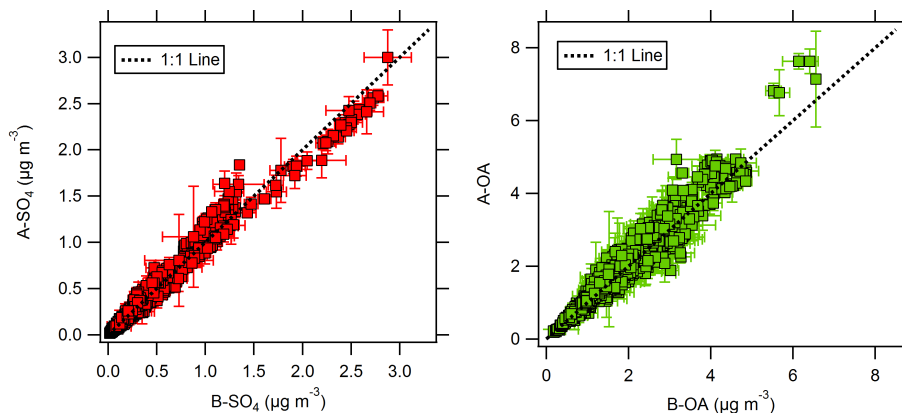
523 <sup>c</sup> Table entries where the null hypothesis ("equal medians") between the above- and below-canopy data cannot be rejected  
 524 and was not statistically significant ( $p > 0.05$ ) using a two-sided, non-parametric Wilcoxon rank-sum test. All other table  
 525 entries indicate that the null hypothesis ("equal medians") can be rejected at the statistical significance level ( $p < 0.05$ ).  
 526

527 concentration near the mid-canopy. Correlation analysis of these secondary oxidation products and HCOOH indicates that  
 528 HCOOH likely originates from a secondary source in this environment (Alwe et al., 2019). In the present study, the overall  
 529 homogeneity in OA factors implies that, despite vertical gradients in trace gases and BVOCs from primary emission and  
 530 secondary production, turbulent mixing of aerosols between the forest canopy and the atmosphere is efficient.

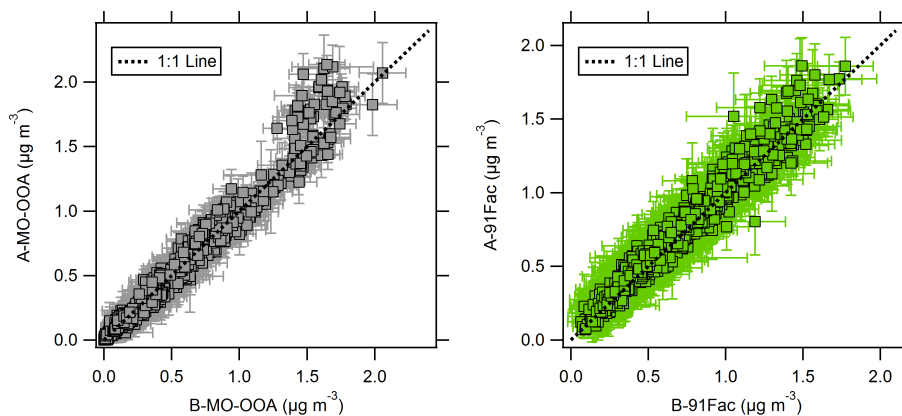
531 Furthermore, this similarity between the above- and below-canopy environments suggests that the chemical timescales  
 532 of SOA formation processes likely are long relative to residence times due to turbulent mixing (Foken et al., 2012), assuming  
 533 relatively constant background levels. Ultimately, the observed similarity agrees with previous modeling work that predicts  
 534 similar SOA mass loadings at these two heights (Ashworth et al., 2015; Schulze et al., 2017). The results shown in the  
 535 present work also are in agreement with measurements at the site in 2009, showing that aerosol gradients on the PROPHET  
 536 tower "existed at times between the above-canopy (31.4m) and understory environments (5 m)," but that the understory  
 537 conditions were generally similar to that of the above-canopy conditions (VanReken et al., 2015). The vertical similarity in



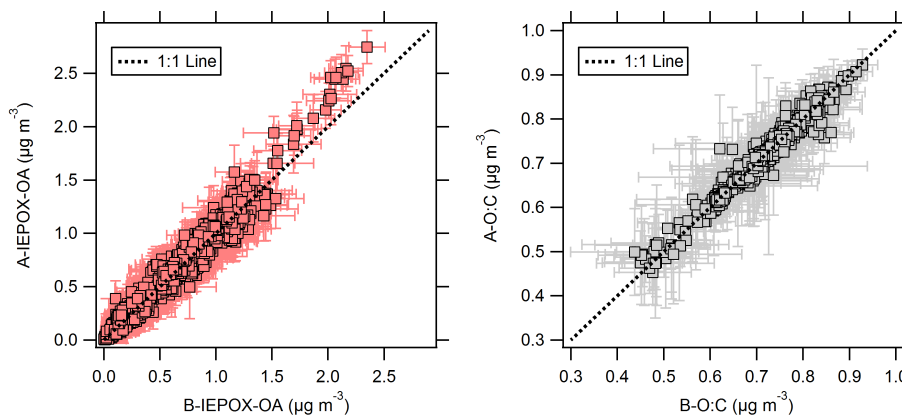
538



539



540



541

542 **Figure 4: Scatter plots of above- (A) and below- (B) canopy hourly-averaged values for: (top from left to right) SO<sub>4</sub>**  
543 **and total OA, (middle from left to right) MO-OOA and 91Fac, and (bottom) IEPOX-OA and campaign O:C. The**  
544 **three-way valve switched between the two inlets at 10-minute intervals, so 30-minute averaged mass concentrations**  
545 **allows for a comparison of both inlets on the same time basis. Above-canopy values are plotted on the y-axis of each**  
546 **plot and below-canopy values are plotted on the x-axis of each plot. Averages are shown with squares; whiskers**  
547 **represent one standard deviation from the mean. For reference, a 1:1 line is shown with each plot. Outliers on the**  
548 **O:C plot corresponding to periods of precipitation were removed.**





549

550 NR-PM<sub>1</sub> is also in agreement with findings in the Amazon forest, where a balance between upward and downward fine  
551 particle fluxes was found (Rizzo et al., 2010) and in a southeast Asian rainforest, where PM<sub>1</sub> did not show significant  
552 variations with height during the daytime (Whitehead et al., 2010).

### 553 3.4.2 Episodes of vertical differences in NR-PM<sub>1</sub>

554 Episodes of vertical differences in NR-PM<sub>1</sub> between the two inlets were observed, and four such episodes are described  
555 here: Episode #1 (Period: 7/3/2016 19:30 to 7/5/2016 15:00 EDT), Episode #2 (July 11 15:00 to July 12 23:00 EDT),  
556 Episode #3 (7/16/2016 21:30 to 7/19/2016 08:30 EDT), and Episode #4 (7/26/2016 08:30 to 7/31/2016 13:30 EDT).  
557 Episodes were defined as sustained periods in which a vertical difference in OA or SO<sub>4</sub> was greater than or equal to  
558 concentrations representing  $\geq 25\%$  of the campaign averaged OA or SO<sub>4</sub>. Episodes #1, #3, and #4 indicate increased above-  
559 canopy OA concentrations, while Episode #2 indicates increased below-canopy SO<sub>4</sub> concentrations. Episodes with higher  
560 above-canopy NR-PM<sub>1</sub> ranged up to  $\sim 1.0 \mu\text{g m}^{-3}$  higher in OA and  $\sim 0.5 \mu\text{g m}^{-3}$  higher in SO<sub>4</sub> relative to equivalent  
561 above/below mass ( $\Delta = 0$ ). Figure 5 shows time series of vertical differences in OA factors and SO<sub>4</sub> and estimates of friction  
562 velocity ( $u^*$ ) at five different heights (not equal to those for the VOC measurements) on the PROPHET tower over the  
563 campaign. Calculated from three-dimensional wind velocity data,  $u^*$  is a function of the shear stress at the surface and is  
564 used in this study as a metric of in-canopy mixing (Equation 5).

565 The “vertical difference,” symbolized as  $\Delta$  in Figure 5, is defined as the difference between above- and below-canopy  
566 values, where the positive convention indicates larger concentrations above the canopy. Episodes of total OA factor vertical  
567 difference ( $\sum\Delta\text{OA Factors}$ ) are shown in Figure 6 with corresponding observations of  $u^*$  and vertical differences in SO<sub>4</sub> and  
568 O<sub>3</sub>. Figure 6 shows that vertical differences in OA correlate with vertical differences in SO<sub>4</sub> for Episodes #1 and #4, while  
569  $\sum\Delta\text{OA Factors}$  during Episode #3 coincides with higher above-canopy O<sub>3</sub> concentrations. Correlations for Episode #2 are  
570 weaker. These episodes have different OA factor composition: MO-OOA contributing a larger percentage during Episode  
571 #1 and #2, 91Fac contributing roughly half in Episode #3, and IEPOX-OA contributing more than half of the total OA  
572 vertical difference in Episode #4.

### 573 3.5 The role of mixing and particulate SO<sub>4</sub> in vertical differences in OA

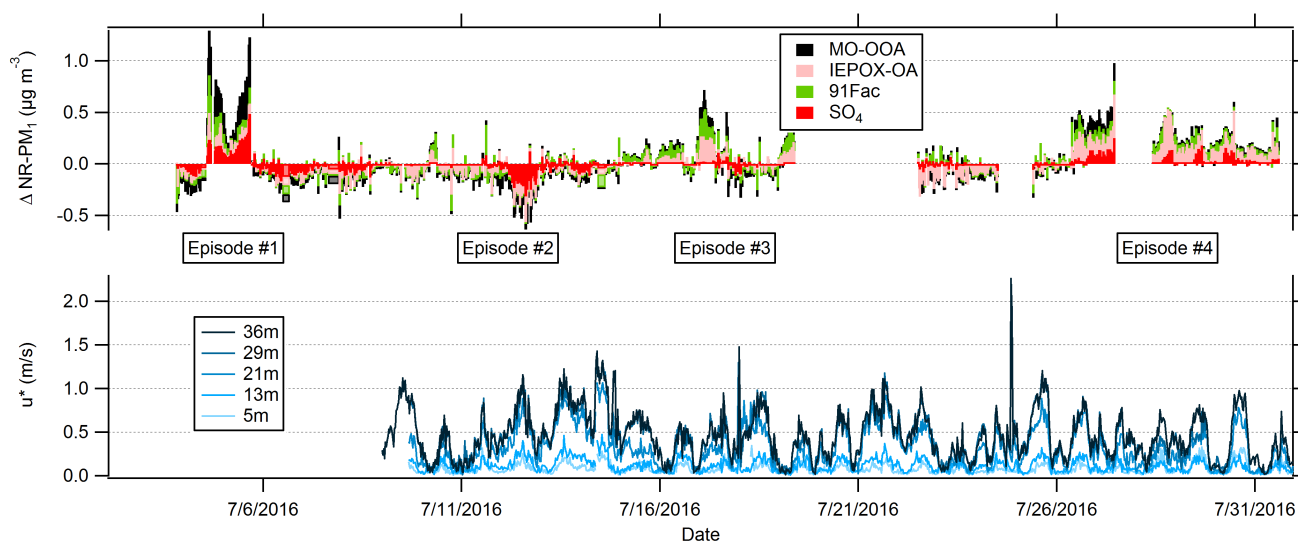
574 The diurnal profile of vertical difference episodes for total OA, SO<sub>4</sub>, and OA factors in 2016 indicate there is no clear  
575 temporal pattern observed for any of these species (Figure S26 in the SI). Maximum vertical differences for SO<sub>4</sub>, total OA,  
576 and MO-OOA are observed around 3PM. For total OA, a gradual increase occurs at 9AM before reaching a maximum  
577 vertical difference at 3PM, suggesting that the episodes of higher above-canopy NR-PM<sub>1</sub> begin shortly after the most  
578 common observed hours of canopy uncoupling from the site in 2009. The initiation of these events may also be attributed to  
579 venting of the nocturnal boundary layer as it breaks up in the morning hours, as observed for events of upward particle  
580 number fluxes by Whitehead et al. (2010).

581 To assess the agreement between the occurrence of episodes and micrometeorological measurements of in-canopy  
582 mixing, episode-specific data for Episodes #2-4 are shown in Figure 6. During Episode #1,  $u^*$  data are available only at  
583 36m, so no friction velocity data are shown, preventing a full analysis similar to those performed for the other three episodes.  
584 However, based on similarity in sulfate enhancements, it can be assumed that Episode #1 is somewhat similar to Episode #4.

585 During Episode #2, based on the backward trajectory cluster analysis shown in Table 1 and the WPSCF results, regional  
586 transport is the likely source of the PM, including the enhancements below canopy. Prior to this episode, SO<sub>4</sub> and MO-OOA  
587 are uniform from below-to-above canopy. The below-canopy enhancement then reaches up to  $0.3 \mu\text{g m}^{-3}$  of SO<sub>4</sub>.  
588 Downmixing of clean air from aloft could lead to lower concentrations above canopy, meaning that the observed difference  
589 would be caused by decreasing above-canopy concentrations, not increasing below-canopy concentrations. However,  
590 below-canopy concentrations are observed to increase while above-canopy concentrations decrease. Without a local, below-

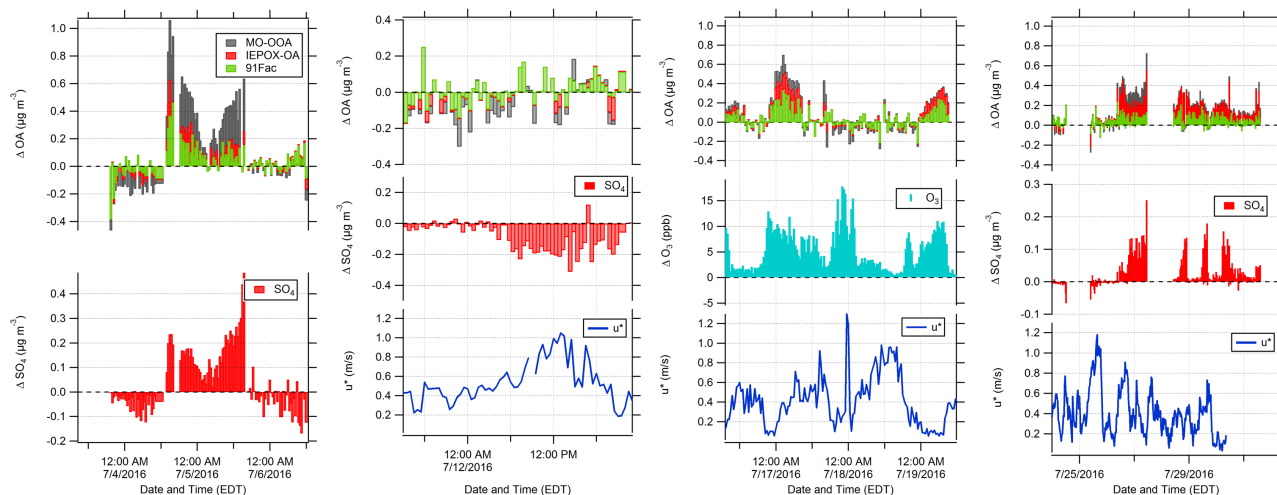


591 canopy source, this indicates that pollutants from above canopy are mixed into the below-canopy region at a rate faster than  
592 they are lost to deposition. Regional pollutants, advected to the site above the boundary layer, can be mixed down to the  
593 surface with daytime boundary layer growth, as has been found in previous aircraft campaigns (Berkowitz et al., 1998;  
594 Thornberry et al., 2001). Downward transport of air masses from the surrounding region has also been hypothesized to  
595 contribute to higher ratios of organic nitrogen to organic carbon ratios in water-soluble aerosols within a forest canopy  
596 relative to its forest floor (Miyazaki et al., 2014).  
597



598  
599 **Figure 5: Time series of (top) observed NR-PM<sub>1</sub> vertical differences between above- and below-canopy inlets and**  
600 **(bottom) friction velocity ( $u^*$ ) in m/s at five different heights on the PROPHET tower. Vertical differences are**  
601 **defined as  $\Delta$  Species, where  $\Delta$  refers to the Above-Canopy minus the Below-Canopy mass concentration. Note that**  
602 **the elevations for  $u^*$  are slightly different than those for trace gas sampling.**  
603

604 During Episodes #3 and #4, periods of above-canopy enhancement in OA factors coincide with relatively lower  $u^*$  ( $u^* <$   
605  $0.2$  m/s during Episode #3 and  $u^* < 0.6$  m/s during Episode #4), with lower friction velocities and greater above-canopy  
606 enhancement in Episode 3. In the case of Episode #3, lower in-canopy mixing, mostly occurring during nighttime, agrees  
607 well with periods of higher above-canopy OA factor and O<sub>3</sub> concentrations. In this case, both IEPOX-OA and 91Fac  
608 contribute to the OA enhancement, likely due to strong photochemistry both locally and during transport (as indicated by  
609 increased O<sub>3</sub>). Episode #4 is the longest duration episode; however, the agreement between low-mixing and above-canopy  
610 PM enhancements is more variable during this case. Similar to Episode #3, the lowest values of friction velocity occur  
611 during the nighttime or early morning. Despite the temporal misalignment of  $\Delta \text{OA}$  and low  $u^*$ , it should be noted that  
612 friction velocities lower than the campaign average ( $\sim 0.4$  m/s) are observed during the latter periods of Episode #4 (7/28-  
613 7/30), which is consistent with the low mixing hypothesis presented for Episode #3. Therefore, it appears that stagnant  
614 conditions above the canopy created an environment where canopy exchange became limited and air masses did not fully  
615 penetrate into the canopy; aerosol deposition below canopy potentially enhanced the positive delta values. This scenario  
616 could also promote in-canopy OA accumulation, but this does not appear to have occurred, implying that other factors  
617 contributed to these vertical differences. Instead, it appears that increased sulfate loading was associated with this transport  
618 and that this increased sulfate above the canopy led to enhancements above canopy, particularly of IEPOX-OA relative to  
619 91Fac, as shown in Figure 6. This also could be related to associated changes in aerosol liquid water.  
620



621

622 **Figure 6: Time series of observed NR-PM<sub>1</sub> vertical difference episodes: (from left to right) Episode #1, Episode #2,**  
 623 **Episode #3, and Episode #4. Data shown for Episode #1, Episode #2, and Episode #4 include vertical differences in**  
 624 **30-minute averaged above- and below-canopy SO<sub>4</sub>, while data shown for Episode #3 show vertical differences in 30-**  
 625 **minute averaged above- and below-canopy O<sub>3</sub>. The O<sub>3</sub> data were measured from the AmeriFlux Tower at 6 meters**  
 626 **and 27 meters and were provided courtesy of CU-Boulder. Friction velocity measurements at 29m on the PROPHET**  
 627 **tower are also provided for Episodes #2-4.**

628

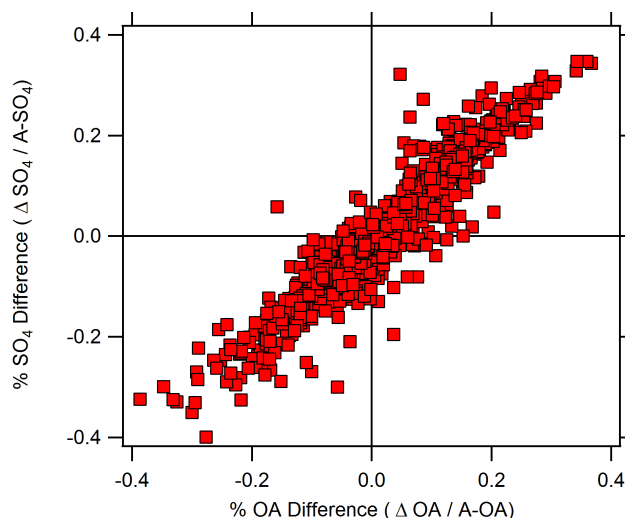
629 The probability distributions of  $\Delta\text{SO}_4$  and  $\Delta\text{O}_3$  between episodes and the average for the entire PROPHET campaign are  
 630 compared in Figure S27 of the SI. The cumulative distribution function (CDF) for  $\Delta\text{SO}_4$  indicates that Episodes #1 and #4  
 631 had higher probabilities of positive  $\Delta\text{SO}_4$  (denoting higher above-canopy concentrations), while Episode #2 had higher  
 632 probabilities of negative  $\Delta\text{SO}_4$  (denoting higher below-canopy concentrations). The episode-specific CDFs for #1 and #2 are  
 633 also different from the total campaign CDF, implying that the vertical differences observed were distinct events. The  
 634 average O<sub>3</sub> difference between the 6- and 27-m inlets on the AmeriFlux tower throughout the campaign indicated that O<sub>3</sub>  
 635 was on average 5 ppb greater at the 27-m inlet, with the difference reaching as high as 34 ppb on July 6 and July 20. The  
 636 probability distribution of vertical O<sub>3</sub> differences observed during Episode #3 is markedly different than those observed  
 637 during Episode #1, Episode #4, and the remainder of the campaign. This indicates that O<sub>3</sub> had a larger probability of being  
 638 between 0-10 ppb higher above the canopy during this episode compared to the rest of the campaign.

639 Based on Episode #1 and Episode #4, a potential driving factor of vertical differences for OA is a vertical difference in  
 640 particulate SO<sub>4</sub>. Figure 7 indicates the vertical differences in OA and SO<sub>4</sub> relative to their respective above-canopy  
 641 concentrations. This metric is defined as “% PM Difference,” where PM is the given PM constituent and is equal to the  
 642  $\Delta\text{PM}$  constituent divided by the above-canopy PM concentration. Data that fall in the upper right and bottom left  
 643 quadrants correspond to higher above- and higher below-canopy concentrations, respectively. The vertical difference above or below  
 644 the canopy can be up to approximately 35% of the total available SO<sub>4</sub> or OA at the site. Figure 7 indicates that there is a  
 645 strong linear relationship between the %SO<sub>4</sub> Difference and %OA Difference during the campaign, even outside of the  
 646 Episodes defined here.

647 The concurrent features of vertical differences in OA factors and SO<sub>4</sub> observed in Episodes #1, #2, and #4 and OA  
 648 factors and O<sub>3</sub> in Episode #3 suggest that long-range regional transport (enhanced MO-OOA, SO<sub>4</sub>, and/or O<sub>3</sub>) is a key first  
 649 step in causing these differences. Local through-canopy mixing then determines whether the enhancement is above  
 650 (Episodes #1, #3, and #4) or below (Episode #2) the canopy. The transported material can then impact local chemistry.  
 651 Increased SO<sub>4</sub> likely increases aerosol hygroscopicity resulting in increased ALW, which could result in increased  
 652 partitioning of semi-volatile organics to the condensed phase (i.e., IEPOX-OA) (Budisulistiorini et al., 2017; El-Sayed et al.,



653 2018; Marais et al., 2016). Pre-existing OA (i.e., MO-OOA) transported with SO<sub>4</sub> aerosol could also play a role in the  
654 partitioning of OA above the canopy during these episodes. Vertical gradients in O<sub>3</sub> coinciding with Episode #3 (higher O<sub>3</sub>  
655 above) could initiate relatively local formation of extremely low volatility compounds, which are first-generation oxidation  
656 products of  $\alpha$ -pinene and O<sub>3</sub> (Jokinen et al., 2015). Based on the WPSCF and backward trajectory clustering results, cooler,  
657 northerly air masses associated with IEPOX-OA also could promote partitioning of semi-volatile organics to the particle  
658 phase. It is important to note that it is difficult to conclude the exact chemical mechanisms that are influencing these events  
659 due to their low mass loadings and episodic nature and the consistently higher above-canopy O<sub>3</sub> concentrations during the  
660 campaign.  
661



662  
663 **Figure 7: Scatter plot of % difference in SO<sub>4</sub> (y-axis) and OA (x-axis) for the entire campaign. The % difference is**  
664 **calculated as  $\Delta$  Species / Above-Canopy Species concentration, and is representative of the normalized  $\Delta$  Species**  
665 **concentration.**

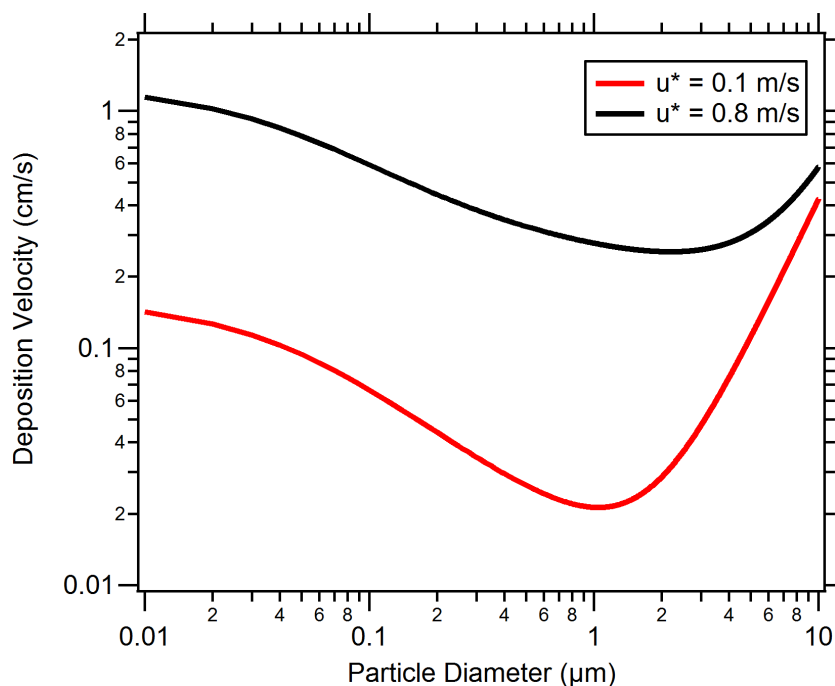
666  
667 Understanding these events is important because uncoupled forest-canopy conditions have been observed in a number of  
668 locations (Foken et al., 2012; Whitehead et al., 2010) and could indicate differences between above-canopy and surface level  
669 PM. One-dimensional modeling has revealed that the timescales of turbulent transport inside a forest canopy can be much  
670 shorter (minutes) than the timescale of aerosol dynamics and deposition (hours) (Rannik et al., 2016), but this evaluation  
671 suggests that advective episodes can cause vertical gradients that are not locally driven. Above-canopy OA and particle  
672 fluxes have been observed in other studies (Farmer et al., 2013; Pryor et al., 2007), suggesting the need for careful evaluation  
673 of whether differences are driven by local chemistry, long-range transport, or a combination thereof.  
674

### 675 3.6 Particle dry deposition model

676 To investigate broadly the effects of canopy mixing on particle deposition in a forest canopy, a particle dry deposition  
677 model is used. Note that we are not applying this through the canopy but to illustrate the relationship between deposition  
678 and  $u^*$ . The resistance model for particle dry deposition assumes that the deposition process is controlled by three  
679 resistances in series: aerodynamic, quasi-laminar, and canopy resistance (Seinfeld and Pandis, 2006). Details on the particle  
680 dry deposition model are included in the SI. Conditions and parameters representative of the land use category, season, and  
681 forest canopy present at the PROPHET site are used as model inputs.

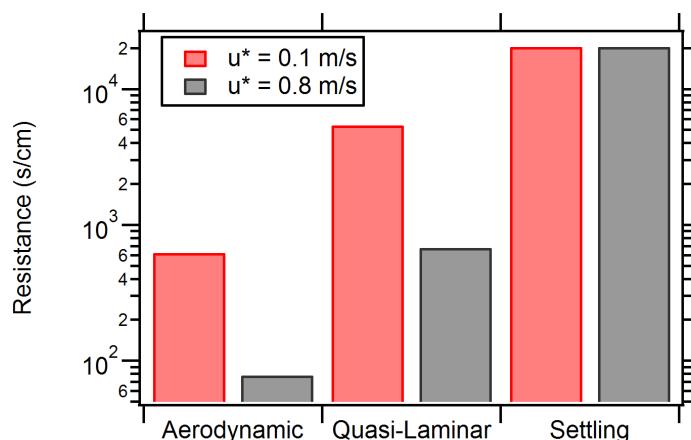


682 Figure 8 displays model results for deposition velocity as a function of particle diameter under stable atmospheric  
683 conditions. For illustration, test cases are shown for  $u^*$  values for low in-canopy mixing ( $u^* = 0.1$  m/s) and high in-canopy  
684 mixing ( $u^* = 0.8$  m/s). Values of  $u^*$  were chosen based on the range of  $u^*$  values observed during the campaign at 29m on  
685 the PROPHET tower. For the submicron particle diameter range (0.1 to 1 micron), a characteristic minimum in deposition  
686 velocity is observed for both test cases at 1 micron diameter. Deposition modeling indicates that higher deposition velocities  
687 are achieved in the high in-canopy mixing test case, implying that there is less canopy transport resistance to the surface and  
688 more deposition in the canopy. This corresponds to Episode #2.  
689



690  
691 **Figure 8: Particle dry deposition velocity resistance model results plotted by particle diameter and friction velocity.**  
692 **Two test cases of low and high friction velocity, representative of data collected at the PROPHET site, are plotted in**  
693 **red and black solid lines, respectively. Land-use conditions and seasonal parameters similar to the PROPHET**  
694 **campaign were used as inputs to the particle dry deposition model. Additional model parameters are provided in the**  
695 **SI.**  
696

697 Deposition modeling also indicates relatively lower deposition velocities for the low mixing condition test case, which  
698 suggests that particles aloft are transported less efficiently into the forest (similar to the conditions present for Episodes #3  
699 and #4). A comparison of the deposition resistances (shown in Figure 9) indicates that aerodynamic and quasi-laminar  
700 resistances in the low-mixing test case are an order of magnitude greater than the high-mixing case. The settling removal  
701 resistance is the same between both test cases because it is merely a function of diameter. A greater aerodynamic resistance  
702 limits turbulent transport from the above-canopy layer to the surface layer and greater quasi-laminar layer resistance limits  
703 transport to just above the surface by lowering particle impaction. In total, this result emphasizes the importance of in-  
704 canopy transport and mixing in governing particle concentrations in forests.  
705



706  
707 **Figure 8: Deposition and particle settling (accounts for the effect of sedimentation) resistances comparison for low**  
708 **and high friction velocities. Resistance comparison assumes a 1 micron particle diameter.**

#### 709 4 Conclusions

710 In this study, source apportionment of OA using separate PMF analyses on inlets situated above and below a forest  
711 canopy resulted in three OA factors at a site in northern Michigan. Similarity in OA composition, concentration, and diurnal  
712 profiles was observed between the two inlets, suggesting that turbulent transport efficiently mixes OA across the canopy.  
713 However, OA factor vertical differences between the two inlets were observed during four separate episodes. During these  
714 episodes, vertical differences were both positive (greater concentrations above the canopy) and negative (greater  
715 concentrations below canopy). NR-PM<sub>1</sub> composition amongst these episodes was unique (Episode #1: MO-OOA dominant,  
716 Episode #2: SO<sub>4</sub> dominant, Episode #3: 91Fac dominant, Episode #4: IEPOX-OA dominant). Furthermore, the vertical  
717 difference concentrations can be 35% of the total available SO<sub>4</sub> or OA at the site. It has also been shown that relative  
718 vertical differences in SO<sub>4</sub> and OA are linearly associated, suggesting the role of regional SO<sub>4</sub> in vertical profiles of NR-PM<sub>1</sub>  
719 in forested environments.

720 Using micrometeorological measurements, it has been hypothesized that periods of low in-canopy mixing  
721 conditions can be associated with the timing of vertical difference episodes where above-canopy concentrations are larger  
722 than those below. The opposite scenario is hypothesized to be associated with transport of air from aloft or with  
723 accumulation of material below canopy more rapidly than it is deposited. Either way, these results suggest that canopy  
724 mixing impacts particle levels. However, under low-mixing scenarios, it appears that enhancements as defined here depend  
725 on both these conditions and the presence of transported O<sub>3</sub> or SO<sub>4</sub> to enhance IEPOX-OA and 91Fac levels.

726 To the knowledge of the author, this is one of only a few studies that have assessed vertical profiles in OA factors  
727 above and below a forest canopy, and the first study to observe episodes of vertical differences in OA factors above and  
728 below a forest canopy. This work adds to the existing literature on aerosol chemistry in a forest canopy environment  
729 presented by Rizzo et al. (2010) and Whitehead et al. (2010) and to literature on vertical profiles of OA in an urban  
730 environment by Özturk et al. (2013).

731 To investigate the effects of forest canopies on SOA formation, small-scale models, such as those described in  
732 Schulze et al. (2017) and Ashworth et al. (2015), have been developed. The OA data from this work can be used to validate  
733 such models and are particularly relevant to these modeling efforts, as the models were developed using campaign data from  
734 the PROPHET site in 2009. Vertical transport and horizontal advection are both sources of uncertainty in current forest  
735 canopy-atmosphere exchange models, which are designed to focus on local processes. Ultimately, the vertical similarity in



736 NR-PM<sub>1</sub> OA composition observed in this study implies that it may be valid to assume that below-canopy OA composition  
737 is generally representative of the OA composition in the atmospheric layer directly above the canopy and vice versa.  
738 However, this work highlights that advection of regional pollution into forested regions can lead to in-canopy gradients that  
739 are not present under purely local conditions.  
740

#### 741 **Data Availability**

742 Data are available through contacting the corresponding author.

#### 743 **Author Contributions**

744 A.A.T.B. prepared the manuscript with input from all authors. A.A.T.B., H.W.W. and R.J.G. conceived of the study and  
745 operated and analyzed the data from the HR-ToF-AMS. S.K. and A.L.S. investigated friction velocity and in-canopy  
746 mixing. H.D.A. and D.B.M. collected and analyzed VOC data. J.H.F., M.H.E. and S.A. collected and analyzed trace gas  
747 data and operated the MAQL.

#### 748 **Competing Interests**

749 The authors declare they have no conflict of interest.

#### 750 **Acknowledgements**

751 The assistance of all staff and collaborators at UMBS is gratefully acknowledged. We would like to thank Wei Wang at  
752 University of Colorado Boulder for assistance in collecting O<sub>3</sub> data at the AmeriFlux tower and the Murphy group at the  
753 University of Toronto for provision of nitrogen oxide data. This work was funded by the National Science Foundation  
754 (NSF) under grant AGS-1552086. PTR-QiToF measurements during PROPHET-AMOS were also supported by NSF (grants  
755 AGS-1428257+AGS-1148951). Trace gas and meteorological measurements on board the MAQL were also supported by  
756 NSF (grant AGS-1552077).

#### 757 **References**

- 758 Alwe, H.D., Millet, D.B., Chen, X., Raff, J.D., Payne, Z.C., Fledderman, K., 2019. Oxidation of Volatile Organic  
759 Compounds as the Major Source of Formic Acid in a Mixed Forest Canopy. *Geophysical Research Letters* 0.  
760 <https://doi.org/10.1029/2018GL081526>
- 761 Ashworth, K., Chung, S.H., Griffin, R.J., Chen, J., Forkel, R., Bryan, A.M., Steiner, A.L., 2015. FORest Canopy  
762 Atmosphere Transfer (FORCAsT) 1.0: a 1-D model of biosphere-atmosphere chemical exchange. *Geoscientific*  
763 *Model Development* 8, 3765–3784. <https://doi.org/10.5194/gmd-8-3765-2015>
- 764 Baldocchi, D., Guenther, A.B., Harley, P., Klinger, L., Zimmerman, P., Lamb, B., Westberg, H., 1995. The fluxes and air  
765 chemistry of isoprene above a deciduous hardwood forest. *Philosophical Transactions: Physical Sciences and*  
766 *Engineering* 351, 279–296.
- 767 Bergen, K.M., Dronova, I., 2007. Observing succession on aspen-dominated landscapes using a remote sensing-ecosystem  
768 approach. *Landscape Ecology* 22, 1395–1410. <https://doi.org/10.1007/s10980-007-9119-1>
- 769 Berkowitz, C.M., Fast, J.D., Springston, S.R., Larsen, R.J., Spicer, C.W., Doskey, P.V., Hubbe, J.M., Plastridge, R., 1998.  
770 Formation mechanisms and chemical characteristics of elevated photochemical layers over the northeast United  
771 States. *J. Geophys. Res.* 103, 10631–10647. <https://doi.org/10.1029/97JD03751>



- 772 Bondy, A.L., Wang, B., Laskin, A., Craig, R.L., Nhliziyo, M.V., Bertman, S., Pratt, K.A., Shepson, P.B., Ault, A.P., 2017.  
773 Inland Sea Spray Aerosol Transport and Incomplete Chloride Depletion: Varying Degrees of Reactive Processing  
774 Observed during SOAS. *Environ. Sci. Technol.* <https://doi.org/10.1021/acs.est.7b02085>
- 775 Brown, S.S., Osthoff, H.D., Stark, H., Dubé, W.P., Ryerson, T.B., Warneke, C., de Gouw, J.A., Wollny, A.G., Parrish, D.D.,  
776 Fehsenfeld, F.C., Ravishankara, A.R., 2005. Aircraft observations of daytime NO<sub>3</sub> and N<sub>2</sub>O<sub>5</sub> and their implications  
777 for tropospheric chemistry. *Journal of Photochemistry and Photobiology A: Chemistry* 176, 270–278.  
778 <https://doi.org/10.1016/j.jphotochem.2005.10.004>
- 779 Bryan, A.M., Bertman, S.B., Carroll, M.A., Dusanter, S., Edwards, G.D., Forkel, R., Griffith, S., Guenther, A.B., Hansen,  
780 R.F., Helmig, D., Jobson, B.T., Keutsch, F.N., Lefer, B.L., Pressley, S.N., Shepson, P.B., Stevens, P.S., Steiner,  
781 A.L., 2012. In-canopy gas-phase chemistry during CABINEX 2009: sensitivity of a 1-D canopy model to vertical  
782 mixing and isoprene chemistry. *Atmospheric Chemistry and Physics* 12, 8829–8849. <https://doi.org/10.5194/acp-12-8829-2012>
- 784 Budisulistiorini, S.H., Nenes, A., Carlton, A.G., Surratt, J.D., McNeill, V.F., Pye, H.O.T., 2017. Simulating Aqueous-Phase  
785 Isoprene-Epoxydiol (IEPOX) Secondary Organic Aerosol Production During the 2013 Southern Oxidant and  
786 Aerosol Study (SOAS). *Environmental Science & Technology* 51, 5026–5034.  
787 <https://doi.org/10.1021/acs.est.6b05750>
- 788 Canagaratna, M.R., Jimenez, J.L., Kroll, J.H., Chen, Q., Kessler, S.H., Massoli, P., Hildebrandt Ruiz, L., Fortner, E.,  
789 Williams, L.R., Wilson, K.R., Surratt, J.D., Donahue, N.M., Jayne, J.T., Worsnop, D.R., 2015. Elemental ratio  
790 measurements of organic compounds using aerosol mass spectrometry: characterization, improved calibration, and  
791 implications. *Atmospheric Chemistry and Physics* 15, 253–272. <https://doi.org/10.5194/acp-15-253-2015>
- 792 Carlton, A.G., Baker, K.R., 2011. Photochemical Modeling of the Ozark Isoprene Volcano: MEGAN, BEIS, and Their  
793 Impacts on Air Quality Predictions. *Environmental Science & Technology* 45, 4438–4445.  
794 <https://doi.org/10.1021/es200050x>
- 795 Carroll, M.A., Bertman, S.B., Shepson, P.B., 2001. Overview of the Program for Research on Oxidants: PHotochemistry,  
796 Emissions, and Transport (PROPHET) summer 1998 measurements intensive. *Journal of Geophysical Research*  
797 106.
- 798 Chang, Y., Deng, C., Cao, F., Cao, C., Zou, Z., Liu, S., Lee, X., Li, J., Zhang, G., Zhang, Y., 2017. Assessment of  
799 carbonaceous aerosols in Shanghai, China – Part 1: long-term evolution, seasonal variations, and meteorological  
800 effects. *Atmos. Chem. Phys.* 17, 9945–9964. <https://doi.org/10.5194/acp-17-9945-2017>
- 801 Cooper, O.R., Moody, J.L., Thornberry, T.D., Town, M.S., Carroll, M.A., 2001. PROPHET 1998 meteorological overview  
802 and air-mass classification. *Journal of Geophysical Research* 106.
- 803 Cubison, M.J., Ortega, A.M., Hayes, P.L., Farmer, D.K., Day, D., Lechner, M.J., Brune, W.H., Apel, E., Diskin, G.S.,  
804 Fisher, J.A., Fuelberg, H.E., Hecobian, A., Knapp, D.J., Mikoviny, T., Riemer, D., Sachse, G.W., Sessions, W.,  
805 Weber, R.J., Weinheimer, A.J., Wisthaler, A., Jimenez, J.L., 2011. Effects of aging on organic aerosol from open  
806 biomass burning smoke in aircraft and laboratory studies. *Atmospheric Chemistry and Physics* 11, 12049–12064.  
807 <https://doi.org/10.5194/acp-11-12049-2011>
- 808 DeCarlo, P.F., Kimmel, J.R., Trimborn, A., Northway, M.J., Jayne, J.T., Aiken, A.C., Gonin, M., Fuhrer, K., Horvath, T.,  
809 Docherty, K.S., others, 2006. Field-deployable, high-resolution, time-of-flight aerosol mass spectrometer.  
810 *Analytical Chemistry* 78, 8281–8289.
- 811 Ditto, J.C., Barnes, E.B., Khare, P., Takeuchi, M., Joo, T., Bui, A.A.T., Lee-Taylor, J., Eris, G., Chen, Y., Aumont, B.,  
812 Jimenez, J.L., Ng, N.L., Griffin, R.J., Gentner, D.R., 2018. An omnipresent diversity and variability in the chemical  
813 composition of atmospheric functionalized organic aerosol. *Communications Chemistry* 1, 75.  
814 <https://doi.org/10.1038/s42004-018-0074-3>
- 815 Draxler, R.R., Hess, G.D., 1998. An overview of the HYSPLIT\_4 modeling system for trajectories, dispersion, and  
816 deposition. *Australian meteorological magazine* 47.
- 817 El-Sayed, M.M.H., Ortiz-Montalvo, D.L., Hennigan, C.J., 2018. The effects of isoprene and NO<sub>x</sub> on secondary organic  
818 aerosols formed through reversible and irreversible uptake to aerosol water. *Atmospheric Chemistry and Physics*  
819 18, 1171–1184. <https://doi.org/10.5194/acp-18-1171-2018>





- 820 Farmer, D.K., Chen, Q., Kimmel, J.R., Docherty, K.S., Nemitz, E., Artaxo, P.A., Cappa, C.D., Martin, S.T., Jimenez, J.L.,  
821 2013. Chemically Resolved Particle Fluxes Over Tropical and Temperate Forests. *Aerosol Science and Technology*  
822 47, 818–830. <https://doi.org/10.1080/02786826.2013.791022>
- 823 Fehsenfeld, F.C., Calvert, J.G., Fall, R., Goldan, P., Guenther, A., Hewitt, C.N., Lamb, B., Shaw, L., Trainer, M., Westberg,  
824 H., Zimmerman, P., 1992. Emissions of volatile organic compounds from vegetation and the implications for  
825 atmospheric chemistry. *Global Biogeochemical Cycles* 6.
- 826 Finnigan, J., 2000. Turbulence in plant canopies. *Annual Review of Fluid Mechanics* 32, 519–571.
- 827 Foken, T., Meixner, F.X., Falge, E., Zetzsch, C., Serafimovich, A., Bargsten, A., Behrendt, T., Biermann, T., Breuninger, C.,  
828 Dix, S., Gerken, T., Hunner, M., Lehmann-Pape, L., Hens, K., Jocher, G., Kesselmeier, J., Lüers, J., Mayer, J.-C.,  
829 Moravek, A., Plake, D., Riederer, M., Rütz, F., Scheibe, M., Siebicke, L., Sörgel, M., Staudt, K., Trebs, I.,  
830 Tsokankunku, A., Welling, M., Wolff, V., Zhu, Z., 2012. Coupling processes and exchange of energy and reactive  
831 and non-reactive trace gases at a forest site – results of the EGER experiment. *Atmospheric Chemistry and Physics*  
832 12, 1923–1950. <https://doi.org/10.5194/acp-12-1923-2012>
- 833 Fuentes, J.D., Wang, D., Bowling, D.R., Potosnak, M., Monson, R.K., Goliff, W.S., Stockwell, W.R., 2007. Biogenic  
834 Hydrocarbon Chemistry within and Above a Mixed Deciduous Forest. *Journal of Atmospheric Chemistry* 56, 165–  
835 185. <https://doi.org/10.1007/s10874-006-9048-4>
- 836 Gao, W., Wesely, M.L., Doskey, P.V., 1993. Numerical modeling of the turbulent diffusion and chemistry of NO<sub>x</sub>, O<sub>3</sub>,  
837 isoprene, and other reactive trace gases in and above a forest canopy. *Journal of Geophysical Research:*  
838 *Atmospheres* 98, 18339–18353. <https://doi.org/10.1029/93JD01862>
- 839 Geron, C., Rasmussen, R., R. Arnsts, R., Guenther, A., 2000. A review and synthesis of monoterpene speciation from forests  
840 in the United States. *Atmospheric Environment* 34, 1761–1781. [https://doi.org/10.1016/S1352-2310\(99\)00364-7](https://doi.org/10.1016/S1352-2310(99)00364-7)
- 841 Goldstein, A.H., Galbally, I.E., 2007. Known and unexplored organic constituents in the earth's atmosphere. *Environmental*  
842 *Science & Technology*.
- 843 Gordon, M., Staebler, R.M., Liggio, J., Vlasenko, A., Li, S.-M., Hayden, K., 2011. Aerosol flux measurements above a  
844 mixed forest at Borden, Ontario. *Atmospheric Chemistry and Physics* 11, 6773–6786. [https://doi.org/10.5194/acp-](https://doi.org/10.5194/acp-11-6773-2011)  
845 [11-6773-2011](https://doi.org/10.5194/acp-11-6773-2011)
- 846 Guenther, A., Geron, C., Pierce, T., Lamb, B., Harley, P., Fall, R., 2000. Natural emissions of non-methane volatile organic  
847 compounds, carbon monoxide, and oxides of nitrogen from North America. *Atmospheric Environment* 34, 2205–  
848 2230.
- 849 Guenther, A., Hewitt, C.N., Erickson, D., Fall, R., Geron, C., Graedel, T., Harley, P., Klinger, L., Lerdau, M., McKay, W.A.,  
850 Pierce, T., Scholes, B., Steinbrecher, R., Tallamraju, R., Taylor, J., Zimmerman, P., 1995. A global model of natural  
851 volatile organic compound emissions. *Journal of Geophysical Research* 100.
- 852 Gunsch, M.J., May, N.W., Wen, M., Bottenus, C.L.H., Gardner, D.J., VanReken, T.M., Bertman, S.B., Hopke, P.K., Ault,  
853 A.P., Pratt, K.A., 2018. Ubiquitous influence of wildfire emissions and secondary organic aerosol on summertime  
854 atmospheric aerosol in the forested Great Lakes region. *Atmospheric Chemistry and Physics* 18, 3701–3715.  
855 <https://doi.org/10.5194/acp-18-3701-2018>
- 856 Holzinger, R., Lee, A., Paw, K.T., Goldstein, U.A.H., 2005. Observations of oxidation products above a forest imply  
857 biogenic emissions of very reactive compounds. *Atmospheric Chemistry and Physics* 5, 67–75.
- 858 Hu, W.W., Campuzano-Jost, P., Palm, B.B., Day, D.A., Ortega, A.M., Hayes, P.L., Krechmer, J.E., Chen, Q., Kuwata, M.,  
859 Liu, Y.J., de Sá, S.S., McKinney, K., Martin, S.T., Hu, M., Budisulistiorini, S.H., Riva, M., Surratt, J.D., St. Clair,  
860 J.M., Isaacman-Van Wertz, G., Yee, L.D., Goldstein, A.H., Carbone, S., Brito, J., Artaxo, P., de Gouw, J.A., Koss,  
861 A., Wisthaler, A., Mikoviny, T., Karl, T., Kaser, L., Jud, W., Hansel, A., Docherty, K.S., Alexander, M.L.,  
862 Robinson, N.H., Coe, H., Allan, J.D., Canagaratna, M.R., Paulot, F., Jimenez, J.L., 2015. Characterization of a real-  
863 time tracer for isoprene epoxydiols-derived secondary organic aerosol (IEPOX-SOA) from aerosol mass  
864 spectrometer measurements. *Atmospheric Chemistry and Physics* 15, 11807–11833. [https://doi.org/10.5194/acp-15-](https://doi.org/10.5194/acp-15-11807-2015)  
865 [11807-2015](https://doi.org/10.5194/acp-15-11807-2015)
- 866 IPCC (Ed.), 2007. *Climate change 2007: the physical science basis: contribution of Working Group I to the Fourth*  
867 *Assessment Report of the Intergovernmental Panel on Climate Change*. Cambridge University Press, Cambridge ;  
868 New York.



- 869 Jimenez, J.L., Canagaratna, M.R., Donahue, N.M., Prevot, A.S.H., Zhang, Q., Kroll, J.H., DeCarlo, P.F., Allan, J.D., Coe,  
870 H., Ng, N.L., Aiken, A.C., Docherty, K.S., Ulbrich, I.M., Grieshop, A.P., Robinson, A.L., Duplissy, J., Smith, J.D.,  
871 Wilson, K.R., Lanz, V.A., Hueglin, C., Sun, Y.L., Tian, J., Laaksonen, A., Raatikainen, T., Rautiainen, J.,  
872 Vaattovaara, P., Ehn, M., Kulmala, M., Tomlinson, J.M., Collins, D.R., Cubison, M.J., Dunlea, E., Huffman, J.A.,  
873 Onasch, T.B., Alfarra, M.R., Williams, P.I., Bower, K., Kondo, Y., Schneider, J., Drewnick, F., Borrmann, S.,  
874 Weimer, S., Demerjian, K., Salcedo, D., Cottrell, L., Griffin, R., Takami, A., Miyoshi, T., Hatakeyama, S.,  
875 Shimono, A., Sun, J.Y., Zhang, Y.M., Dzepina, K., Kimmel, J.R., Sueper, D., Jayne, J.T., Herndon, S.C., Trimborn,  
876 A.M., Williams, L.R., Wood, E.C., Middlebrook, A.M., Kolb, C.E., Baltensperger, U., Worsnop, D.R., 2009.  
877 Evolution of Organic Aerosols in the Atmosphere. *Science* 326, 1525–1529.  
878 <https://doi.org/10.1126/science.1180353>
- 879 Jokinen, T., Berndt, T., Makkonen, R., Kerminen, V.-M., Junninen, H., Paasonen, P., Stratmann, F., Herrmann, H.,  
880 Guenther, A.B., Worsnop, D.R., Kulmala, M., Ehn, M., Sipilä, M., 2015. Production of extremely low volatile  
881 organic compounds from biogenic emissions: Measured yields and atmospheric implications. *Proceedings of the*  
882 *National Academy of Sciences* 112, 7123–7128. <https://doi.org/10.1073/pnas.1423977112>
- 883 Kanakidou, M., Seinfeld, J.H., Pandis, S.N., Barnes, I., Dentener, F.J., Facchini, M.C., Dingenen, R.V., Ervens, B., Nenes,  
884 A., Nielsen, C.J., others, 2005. Organic aerosol and global climate modelling: a review. *Atmospheric Chemistry and*  
885 *Physics* 5, 1053–1123.
- 886 Kroll, J.H., Donahue, N.M., Jimenez, J.L., Kessler, S.H., Canagaratna, M.R., Wilson, K.R., Altieri, K.E., Mazzoleni, L.R.,  
887 Wozniak, A.S., Bluhm, H., Mysak, E.R., Smith, J.D., Kolb, C.E., Worsnop, D.R., 2011. Carbon oxidation state as a  
888 metric for describing the chemistry of atmospheric organic aerosol. *Nature Chemistry* 3, 133–139.  
889 <https://doi.org/10.1038/nchem.948>
- 890 Kruijt, B., Malhi, Y., Lloyd, J., Norbre, A.D., Miranda, A.C., Pereira, M.G.P., Culf, A., Grace, J., 2000. Turbulence  
891 Statistics Above And Within Two Amazon Rain Forest Canopies. *Boundary-Layer Meteorology* 94, 297–331.  
892 <https://doi.org/10.1023/A:1002401829007>
- 893 Leong, Y.J., Sanchez, N.P., Wallace, H.W., Cevik, B.K., Hernandez, C.S., Han, Y., Flynn, J.H., Massoli, P., Flerchinger,  
894 C., Fortner, E.C., Herndon, S., Bean, J.K., Ruiz, L.H., Jeon, W., Choi, Y., Lefer, B., Griffin, R.J., 2017. Overview  
895 of surface measurements and spatial characterization of submicrometer particulate matter during the DISCOVER-  
896 AQ 2013 campaign in Houston, TX. *Journal of the Air & Waste Management Association* 67, 854–872.  
897 <https://doi.org/10.1080/10962247.2017.1296502>
- 898 Makar, P.A., Staebler, R.M., Akingunola, A., Zhang, J., McLinden, C., Kharol, S.K., Pabla, B., Cheung, P., Zheng, Q., 2017.  
899 The effects of forest canopy shading and turbulence on boundary layer ozone. *Nature Communications* 8, 15243,  
900 <https://doi.org/10.1038/ncomms15243>
- 901 Marais, E.A., Jacob, D.J., Jimenez, J.L., Campuzano-Jost, P., Day, D.A., Hu, W., Krechmer, J., Zhu, L., Kim, P.S., Miller,  
902 C.C., Fisher, J.A., Travis, K., Yu, K., Hanisco, T.F., Wolfe, G.M., Arkinson, H.L., Pye, H.O.T., Froyd, K.D., Liao,  
903 J., McNeill, V.F., 2016. Aqueous-phase mechanism for secondary organic aerosol formation from isoprene:  
904 application to the southeast United States and co-benefit of SO<sub>2</sub> emission controls. *Atmospheric Chemistry and*  
905 *Physics* 16, 1603–1618. <https://doi.org/10.5194/acp-16-1603-2016>
- 906 Middlebrook, A.M., Bahreini, R., Jimenez, J.L., Canagaratna, M.R., 2012. Evaluation of Composition-Dependent Collection  
907 Efficiencies for the Aerodyne Aerosol Mass Spectrometer using Field Data. *Aerosol Science and Technology* 46,  
908 258–271. <https://doi.org/10.1080/02786826.2011.620041>
- 909 Millet, D.B., Alwe, H.D., Chen, X., Deventer, M.J., Griffis, T.J., Holzinger, R., Bertman, S.B., Rickly, P.S., Stevens, P.S.,  
910 Léonardis, T., Locoge, N., Dusanter, S., Tyndall, G.S., Alvarez, S.L., Erickson, M.H., Flynn, J.H., 2018.  
911 Bidirectional Ecosystem–Atmosphere Fluxes of Volatile Organic Compounds Across the Mass Spectrum: How  
912 Many Matter? *ACS Earth and Space Chemistry* 2, 764–777. <https://doi.org/10.1021/acsearthspacechem.8b00061>
- 913 Miyazaki, Y., Fu, P., Ono, K., Tachibana, E., Kawamura, K., 2014. Seasonal cycles of water-soluble organic nitrogen  
914 aerosols in a deciduous broadleaf forest in northern Japan. *J. Geophys. Res. Atmos.* 119, 1440–1454.  
915 <https://doi.org/10.1002/2013JD020713>
- 916 Mohr, C., DeCarlo, P.F., Heringa, M.F., Chirico, R., Slowik, J.G., Richter, R., Reche, C., Alastuey, A., Querol, X., Seco, R.,  
917 Peñuelas, J., Jiménez, J.L., Crippa, M., Zimmermann, R., Baltensperger, U., Prévôt, A.S.H., 2012. Identification



- 918 and quantification of organic aerosol from cooking and other sources in Barcelona using aerosol mass spectrometer  
919 data. *Atmospheric Chemistry and Physics* 12, 1649–1665. <https://doi.org/10.5194/acp-12-1649-2012>
- 920 NADP, 2016. National Atmospheric Deposition Program, National Trends Network (NTN) Site Details [WWW Document].  
921 URL <http://nadp.slh.wisc.edu/data/sites/siteDetails.aspx?net=NTN&id=MI09> (accessed 6.21.18).
- 922 Ng, N.L., Canagaratna, M.R., Zhang, Q., Jimenez, J.L., Tian, J., Ulbrich, I.M., Kroll, J.H., Docherty, K.S., Chhabra, P.S.,  
923 Bahreini, R., Murphy, S.M., Seinfeld, J.H., Hildebrandt, L., Donahue, N.M., DeCarlo, P.F., Lanz, V.A., Prévôt,  
924 A.S.H., Dinar, E., Rudich, Y., Worsnop, D.R., 2010. Organic aerosol components observed in Northern  
925 Hemispheric datasets from Aerosol Mass Spectrometry. *Atmospheric Chemistry and Physics* 10, 4625–4641.  
926 <https://doi.org/10.5194/acp-10-4625-2010>
- 927 Öztürk, F., Bahreini, R., Wagner, N.L., Dubé, W.P., Young, C.J., Brown, S.S., Brock, C.A., Ulbrich, I.M., Jimenez, J.L.,  
928 Cooper, O.R., Middlebrook, A.M., 2013. Vertically resolved chemical characteristics and sources of submicron  
929 aerosols measured on a Tall Tower in a suburban area near Denver, Colorado in winter. *J. Geophys. Res. Atmos.*  
930 118, 2013JD019923. <https://doi.org/10.1002/2013JD019923>
- 931 Paatero, P., 1997. Least squares formulation of robust non-negative factor analysis. *Chemometrics and Intelligent Laboratory*  
932 *Systems* 7, 23–35.
- 933 Paatero, P., Tapper, U., 1994. Positive matrix factorization: A non-negative factor model with optimal utilization of error  
934 estimates of data values. *Environmetrics* 5, 111–126.
- 935 Polissar, A., 1999. The aerosol at Barrow, Alaska: long-term trends and source locations. *Atmospheric Environment* 33,  
936 2441–2458. [https://doi.org/10.1016/S1352-2310\(98\)00423-3](https://doi.org/10.1016/S1352-2310(98)00423-3)
- 937 Polissar, A.V., Hopke, P.K., Harris, J.M., 2001. Source Regions for Atmospheric Aerosol Measured at Barrow, Alaska.  
938 *Environ. Sci. Technol.* 35, 4214–4226. <https://doi.org/10.1021/es0107529>
- 939 Pryor, S.C., Larsen, S.E., Sørensen, L.L., Barthelmie, R.J., Grönholm, T., Kulmala, M., Launiainen, S., Rannik, Ü., Vesala,  
940 T., 2007. Particle fluxes over forests: Analyses of flux methods and functional dependencies. *Journal of*  
941 *Geophysical Research* 112. <https://doi.org/10.1029/2006JD008066>
- 942 Pugh, T. a. M., MacKenzie, A.R., Hewitt, C.N., Langford, B., Edwards, P.M., Furneaux, K.L., Heard, D.E., Hopkins, J.R.,  
943 Jones, C.E., Karunaharan, A., Lee, J., Mills, G., Misztal, P., Moller, S., Monks, P.S., Whalley, L.K., 2010.  
944 Simulating atmospheric composition over a South-East Asian tropical rainforest: performance of a chemistry box  
945 model. *Atmospheric Chemistry and Physics* 10, 279–298. <https://doi.org/10.5194/acp-10-279-2010>
- 946 Rannik, Ü., Zhou, L., Zhou, P., Gierens, R., Mammarella, I., Sogachev, A., Boy, M., 2016. Aerosol dynamics within and  
947 above forest in relation to turbulent transport and dry deposition. *Atmospheric Chemistry and Physics* 16, 3145–  
948 3160. <https://doi.org/10.5194/acp-16-3145-2016>
- 949 Rizzo, L.V., Artaxo, P., Karl, T., Guenther, A.B., Greenberg, J., 2010. Aerosol properties, in-canopy gradients, turbulent  
950 fluxes and VOC concentrations at a pristine forest site in Amazonia. *Atmospheric Environment* 44, 503–511.  
951 <https://doi.org/10.1016/j.atmosenv.2009.11.002>
- 952 Schulze, B.C., Wallace, H.W., Bui, A.T., Flynn, J.H., Erickson, M.H., Alvarez, S., Dai, Q., Usenko, S., Sheesley, R.J.,  
953 Griffin, R.J., 2018. The impacts of regional shipping emissions on the chemical characteristics of coastal submicron  
954 aerosols near Houston, TX. *Atmospheric Chemistry and Physics* 18, 14217–14241. <https://doi.org/10.5194/acp-18-14217-2018>
- 955
- 956 Schulze, B.C., Wallace, H.W., Flynn, J.H., Lefer, B.L., Erickson, M.H., Jobson, B.T., Dusanter, S., Griffith, S.M., Hansen,  
957 R.F., Stevens, P.S., VanReken, T., Griffin, R.J., 2017. Differences in BVOC oxidation and SOA formation above  
958 and below the forest canopy. *Atmospheric Chemistry and Physics* 17, 1805–1828. <https://doi.org/10.5194/acp-17-1805-2017>
- 959
- 960 Seinfeld, J.H., Pandis, S.N., 2006. *Atmospheric chemistry and physics : from air pollution to climate change*. Hoboken, N.J. :  
961 John Wiley, ©2006.
- 962 Sheesley, R.J., Schauer, J.J., Bean, E., Kenski, D., 2004. Trends in Secondary Organic Aerosol at a Remote Site in  
963 Michigan's Upper Peninsula. *Environmental Science & Technology* 38, 6491–6500.  
964 <https://doi.org/10.1021/es049104q>
- 965 Sirois, A., Bottenheim, J.W., 1995. Use of backward trajectories to interpret the 5-year record of PAN and O<sub>3</sub> ambient air  
966 concentrations at Kejimikujik National Park, Nova Scotia. *Journal of Geophysical Research* 100, 2867.  
967 <https://doi.org/10.1029/94JD02951>



- 968 Stein, A.F., Draxler, R.R., Rolph, G.D., Stunder, B.J.B., Cohen, M.D., Ngan, F., 2015. NOAA's HYSPLIT Atmospheric  
969 Transport and Dispersion Modeling System. *Bulletin of the American Meteorological Society* 96, 2059–2077.  
970 <https://doi.org/10.1175/BAMS-D-14-00110.1>
- 971 Steiner, A.L., Pressley, S.N., Botros, A., Jones, E., Chung, S.H., Edburg, S.L., 2011. Analysis of coherent structures and  
972 atmosphere-canopy coupling strength during the CABINEX field campaign. *Atmospheric Chemistry and Physics*  
973 11, 11921–11936. <https://doi.org/10.5194/acp-11-11921-2011>
- 974 Stroud, C., Makar, P., Karl, T., Guenther, A., Geron, C., Turnipseed, A., Nemitz, E., Baker, B., Potosnak, M., Fuentes, J.D.,  
975 2005. Role of canopy-scale photochemistry in modifying biogenic-atmosphere exchange of reactive terpene  
976 species: Results from the CELTIC field study. *Journal of Geophysical Research: Atmospheres* 110.  
977 <https://doi.org/10.1029/2005JD005775>
- 978 Thomas, C., Foken, T., 2007. Flux contribution of coherent structures and its implications for the exchange of energy and  
979 matter in a tall spruce canopy. *Boundary-Layer Meteorology* 123, 317–337. <https://doi.org/10.1007/s10546-006-9144-7>
- 980
- 981 Thornberry, T., Carroll, M.A., Keeler, G.A., Sanford, S., Bertman, S.B., Pippin, M.R., Ostling, K., Grossenbacher, J.W.,  
982 Shepson, P.B., Cooper, O.R., Moody, J.L., Stockwell, W.R., 2001. Observations of reactive oxidized nitrogen and  
983 speciation of NO<sub>y</sub> during the PROPHET summer 1998 intensive. *Journal of Geophysical Research* 106, 359–386.
- 984 Toma, S., Bertman, S., 2012. The atmospheric potential of biogenic volatile organic compounds from needles of white pine  
985 (*Pinus strobus*) in Northern Michigan. *Atmospheric Chemistry and Physics* 12, 2245–2252.  
986 <https://doi.org/10.5194/acp-12-2245-2012>
- 987 Ulbrich, I.M., Canagaratna, M.R., Zhang, Q., Worsnop, D.R., Jimenez, J.L., 2009. Interpretation of organic components  
988 from Positive Matrix Factorization of aerosol mass spectrometric data. *Atmospheric Chemistry and Physics* 9,  
989 2891–2918.
- 990 US Census Bureau, 2018. City and Town Population Totals: 2010-2016 [WWW Document]. URL  
991 <https://www.census.gov/data/tables/2016/demo/popest/total-cities-and-towns.html> (accessed 1.24.18).
- 992 VanReken, T.M., Mwaniki, G.R., Wallace, H.W., Pressley, S.N., Erickson, M.H., Jobson, B.T., Lamb, B.K., 2015. Influence  
993 of air mass origin on aerosol properties at a remote Michigan forest site. *Atmospheric Environment* 107, 35–43.  
994 <https://doi.org/10.1016/j.atmosenv.2015.02.027>
- 995 Wallace, H.W., Sanchez, N.P., Flynn, J.H., Erickson, M.H., Lefer, B.L., Griffin, R.J., 2018. Source apportionment of  
996 particulate matter and trace gases near a major refinery near the Houston Ship Channel. *Atmospheric Environment*  
997 173, 16–29. <https://doi.org/10.1016/j.atmosenv.2017.10.049>
- 998 Wang, Y.Q., 2014. MeteoInfo: GIS software for meteorological data visualization and analysis: Meteorological GIS  
999 software. *Meteorological Applications* 21, 360–368. <https://doi.org/10.1002/met.1345>
- 1000 Wang, Y.Q., Zhang, X.Y., Draxler, R.R., 2009. TrajStat: GIS-based software that uses various trajectory statistical analysis  
1001 methods to identify potential sources from long-term air pollution measurement data. *Environmental Modelling &*  
1002 *Software* 24, 938–939. <https://doi.org/10.1016/j.envsoft.2009.01.004>
- 1003 Whitehead, J.D., Gallagher, M.W., Dorsey, J.R., Robinson, N., Gabey, A.M., Coe, H., McFiggans, G., Flynn, M.J., Ryder,  
1004 J., Nemitz, E., Davies, F., 2010. Aerosol fluxes and dynamics within and above a tropical rainforest in South-East  
1005 Asia. *Atmospheric Chemistry and Physics* 10, 9369–9382. <https://doi.org/10.5194/acp-10-9369-2010>
- 1006 Wiedinmyer, C., Greenberg, J., Guenther, A., Hopkins, B., Baker, K., Geron, C., Palmer, P.I., Long, B.P., Turner, J.R.,  
1007 Pétron, G., Harley, P., Pierce, T.E., Lamb, B., Westberg, H., Baugh, W., Koerber, M., Janssen, M., 2005. Ozarks  
1008 Isoprene Experiment (OZIE): Measurements and modeling of the “isoprene volcano.” *Journal of Geophysical*  
1009 *Research: Atmospheres* 110. <https://doi.org/10.1029/2005JD005800>
- 1010 Wolfe, G.M., Thornton, J.A., 2011. The Chemistry of Atmosphere-Forest Exchange (CAFE) Model – Part 1: Model  
1011 description and characterization. *Atmospheric Chemistry and Physics* 11, 77–101. <https://doi.org/10.5194/acp-11-77-2011>
- 1012
- 1013 Xu, L., Pye, H.O.T., He, J., Chen, Y.L., Murphy, B.N., Ng, N.L., 2018. Experimental and model estimates of the  
1014 contributions from biogenic monoterpenes and sesquiterpenes to secondary organic aerosol in the southeastern  
1015 United States. *Atmospheric Chemistry and Physics* 18, 12613–12637. <https://doi.org/10.5194/acp-18-12613-2018>
- 1016 Xu, L., Suresh, S., Guo, H., Weber, R.J., Ng, N.L., 2015. Aerosol characterization over the southeastern United States using  
1017 high-resolution aerosol mass spectrometry: spatial and seasonal variation of aerosol composition and sources with a



- 1018 focus on organic nitrates. *Atmospheric Chemistry and Physics* 15, 7307–7336. <https://doi.org/10.5194/acp-15-7307->  
1019 2015
- 1020 Zhang, Q., Jimenez, J.L., Canagaratna, M.R., Allan, J.D., Coe, H., Ulbrich, I., Alfarra, M.R., Takami, A., Middlebrook,  
1021 A.M., Sun, Y.L., Dzepina, K., Dunlea, E., Docherty, K., DeCarlo, P.F., Salcedo, D., Onasch, T., Jayne, J.T.,  
1022 Miyoshi, T., Shimo, A., Hatakeyama, S., Takegawa, N., Kondo, Y., Schneider, J., Drewnick, F., Borrmann, S.,  
1023 Weimer, S., Demerjian, K., Williams, P., Bower, K., Bahreini, R., Cottrell, L., Griffin, R.J., Rautiainen, J., Sun,  
1024 J.Y., Zhang, Y.M., Worsnop, D.R., 2007. Ubiquity and dominance of oxygenated species in organic aerosols in  
1025 anthropogenically-influenced Northern Hemisphere midlatitudes: Ubiquity and dominance of oxygenated OA.  
1026 *Geophysical Research Letters* 34, 6. <https://doi.org/10.1029/2007GL029979>
- 1027 Zhang, Q., Jimenez, J.L., Canagaratna, M.R., Ulbrich, I.M., Ng, N.L., Worsnop, D.R., Sun, Y., 2011. Understanding  
1028 atmospheric organic aerosols via factor analysis of aerosol mass spectrometry: a review. *Analytical and*  
1029 *Bioanalytical Chemistry* 401, 3045–3067. <https://doi.org/10.1007/s00216-011-5355-y>
- 1030 Zhang, Q., Worsnop, D.R., Canagaratna, M.R., Jimenez, J.L., 2005. Hydrocarbon-like and oxygenated organic aerosols in  
1031 Pittsburgh: insights into sources and processes of organic aerosols. *Atmospheric Chemistry and Physics* 5, 3289–  
1032 3311.